

This is a post-print version of the manuscript. For the final published version, please refer to *Soft Robotics* at <https://www.liebertpub.com/doi/10.1089/soro.2017.0126>

Title:

Untethered miniature soft robots: Modeling and design of a millimeter-scale swimming magnetic sheet

Running Title:

Untethered Soft Swimming Magnetic Sheet

Authors:

Jiachen Zhang, and Eric Diller

Affiliations:

J. Zhang and E. Diller are with the Department of Mechanical and Industrial Engineering, the University of Toronto, Toronto, Ontario, M5S 3G8 Canada

Correspondence:

Eric Diller, ediller@mie.utoronto.ca

Abstract

The actuation and control of miniature soft robots are challenging problems due to their limited onboard space and flexible bodies. Smart magnetic materials are promising candidates to address these challenges since they can be powered and guided remotely by magnetic field for functionalities such as swimming, grasping, and pumping. Here, we program an undulatory swimming gait into a small rectangular sheet that is made of a flexible magnetic homogeneous composite. The sheet bears a sinusoidal magnetization profile throughout its body and deforms into undulatory shapes in a rotating uniform magnetic field that aligns with its length. The traveling wave like deformation of the sheet interacts with the surrounding liquid and propels the sheet in a bidirectional non-holonomic swimming gait. Previous studies on this sheet were not able to model the deformation accurately or characterize the swimming systematically due to a lack of understanding of the underlying physical principles involved. For the first time, we develop a model from underlying physical principles to explain and predict the sheet deformation, which enables it to swim at air-water interfaces and generate propulsive forces under water with an additional stiff frame. The swimming capability and maneuverability of the millimeter-scale sheet are demonstrated in experiments, and its swimming performances in various scenarios are characterized quantitatively. The soft swimming sheet can potentially be used for microrobotic tasks such as delivering cargo or transporting individual cells in poorly accessible workspaces.

Keywords: soft robotics, undulatory swimming, miniature swimmer, magnetic actuation, microrobotics

1 Introduction

Unlike conventional actuators and sensors that require specific components and structures, smart materials possess functionalities which are inherent to the materials themselves. These materials such as piezoelectric ceramics,¹ shape memory alloy,² electroactive polymers,³ and others are often used to induce motions from an input signal and have thus found use in areas like robotics, astronautics, and bioengineering. Recently, a smart magnetic composite has been demonstrated which consists of a flexible elastomer material with embedded magnetic microparticles.⁴ When the embedded magnetic particles are magnetized in a spatially-varying pattern, complex deformations can be produced from the composite by applying an actuating uniform magnetic field which creates magnetic moments within the composite.⁵⁻⁷

Small-scale magnetic actuators have been proposed before, such as the artificial bacterial flagella presented by Zhang et al.⁸ Most existing small-scale magnetic actuators have distinct magnetic elements connected in one way or another. In contrast, this smart magnetic material, when used as an actuator in micro-scale robotics, can achieve motions like flexing⁹⁻¹¹ and traveling wave swimming propulsion.^{4,12,13} These motions root from the magnetization that is programmed throughout the material volume, leading to simple mechanisms, where the behavior of a device is inherent to the programmed material. The creation of complex motions at the millimeter or smaller size scales is an ongoing challenge in the robotics community, which seeks to miniaturize the mechanism capabilities such as locomotion and manipulation possessed by larger robots. Introducing these functional materials into microrobotics opens new possibilities for device locomotion,^{4,14-16} cargo delivery,¹⁷⁻²⁰ and microobject manipulation.^{10,11,21,22} These functional microrobots find a wide range of applications in biomedicine.²³⁻²⁶ Magnetic actuation is appealing for these applications due to the ability of magnetic fields to penetrate most materials, its biocompatibility, and capacity to generate both forces and torques remotely and quickly.

In the smart magnetic material studied here, permanent magnetic microparticles are embedded into an elastomer matrix, providing volumetrically-distributed forces and/or torques in the presence of an externally-applied magnetic field. These forces and torques deform the material in a predictable manner depending on the spatial magnetization profile of the magnetic particles within the material. If the magnetization profile can be arbitrarily patterned, there is a large reservoir of potential shape deformations of this soft magnetic composite and these deformations can be used to achieve desired micro-device functionalities. In previous works, microgrippers were built using this soft magnetic composite, whose shape change is employed to grip-and-release microobjects and assemble them into three dimensional (3D) structures,^{9-11,27} while other instances of actuating soft matter with magnetic torques were reviewed by Erb et al.²⁸ Predicting and designing the shape of these devices have been explored under some conditions such as a beam bending under a fixed-free boundary condition.⁶

Robotic swimming has been extensively studied at various size scales.^{6,29-31} The swimming of miniature robots is especially challenging due to the fact that time-reversible motions do not result in net propulsive forces (Purcell's Scallop Theorem) and the limited onboard space of miniature robots which prevents them from carrying power or drive systems. Inspired by the vast variety of microorganisms, researchers have proposed several devices capable of the undulatory swimming gait, most of which are actuated by light.³²⁻³⁵ Mathematical analyses have suggested that the swimming speed is roughly proportional to the traveling wave frequency, the square of the wave amplitude, and the reciprocal of the wavelength.^{36,37} For a given input energy, a traveling sinusoidal wave is considered to be the optimal pattern for undulatory swimming.

Previously, we have achieved the undulatory swimming gait on a soft magnetic sheet bearing a sinusoidal magnetization profile, proposed a phenomenologically derived shape model, and developed controllers for swimming speed and direction control.^{4,12,13} However, our previous studies did not explore the underlying physical principles of the sheet deformation, which was assumed to be a sinusoidal shape for simplicity. This sinusoidal deformation assumption did not allow previous works to explain why the sheet was unable to swim effectively underwater or propose a solution.

Compared with direct magnetic pulling, this biomimetic undulatory swimming gait is not only scientifically interesting, but also possesses advantageous capabilities. For example, two undulatory swimming devices can be independently positioned on a two-dimensional (2D) plane and manipulated to follow uncoupled way-point sets.¹³ The swimming speed of such a sheet is shown to be up to 10 body lengths per second, about the same with direct pulling a uniformly magnetized sheet with similar sizes using the same setup. This speed is comparable with other mobile miniature devices, such as helical swimmers²⁰ and biohybrid devices³⁸. From a practical perspective, uniform magnetic fields are often easier to characterize and control than nonuniform magnetic fields, whether the field is created by electromagnetic coils or permanent magnets. In the community, the development of miniature locomotion strategies using uniform magnetic fields attracts significantly more attention than the direct pulling using magnetic field gradient.

Hu et al. explored the multimodal locomotion of a similar soft magnetic sheet.⁷ They focused on controlling the sheet to exhibit various locomotion gaits, including swimming, walking, crawling, and jumping, in a hybrid liquid-solid environment. The undulatory swimming gait was employed when the

sheet was at an air-water interface. In addition, a jellyfish-like time-symmetric motion was utilized to achieve under-water locomotion. Their presented model analyzed the sheet deformation in response to the magnetic torques induced by the applied magnetic field. However, this model is not suitable for on-water undulatory swimming because, when the sheet is at an air-water interface, the surface tension force plays a non-negligible role in determining the sheet shape and cannot be omitted.

In this work, we develop a deformation model from first principles, i.e., underlying physical principles, to describe the sheet behavior when it is located at an air-water interface. The model considers all pertinent factors and shows that the magnetic torques and the surface tension forces play the most and the second most important roles in deforming the swimmer, respectively. The sheet deformations in different scenarios are quantitatively characterized with respect to their similarities with traveling sinusoidal waves. Based on these results, we propose an under-water swimmer that generates propulsive forces inside water with time-irreversible deformation that approximates a traveling sinusoidal wave. We actuate and control the swimming of a soft magnetic sheet at an air-water interface. The sheet swims relying on the programmed magnetization in its material, while maintaining a simple body structure for easy scaling down for microrobotics tasks. The programmed magnetization profile on the sheet is measured for the first time. This work explores the undulatory swimming on a geometric simple magnetic sheet, which can be used in future soft robotic designs as end effectors or actuators. The analysis and modeling of the sheet shape from underlying physical principles provide insights into designing and achieving the undulatory swimming gait, which is time-irreversible and thus appropriate for the low Reynolds number regime.

2 Swimmer Concept

The swimming soft magnetic composite sheet is referred to as the swimmer hereafter. This paper investigates two kinds of swimmers, i.e., on-water swimmers and under-water swimmers, which work at air-water interfaces and under water, respectively. This section explains their concepts and working principles.

2.1 On-Water Swimmer

An on-water swimmer consists of a rectangular sheet of the homogeneous soft magnetic composite. It is constrained to a horizontal air-water interface by surface tensions. A sinusoidal magnetization profile is programmed throughout the swimmer body to endow the swimmer with the swimming ability. This magnetization profile is drawn in **Fig. 1(a)** and **(b)** and described by

$$\vec{M}(x) = M \cos\left(\frac{2\pi x}{\lambda}\right) \hat{i} + M \sin\left(\frac{2\pi x}{\lambda}\right) \hat{k} \quad (1)$$

where M is the magnetization amplitude (unit Ampere per meter), and λ is the sinusoidal wavelength (unit meter). Vector \hat{i} and \hat{k} are the unit vectors of axis x and z of the local coordinate frame, respectively. When a uniform magnetic field \vec{B} (unit Tesla), which does not exceed the magnetic particle coercivity, is applied, the swimmer experiences a volumetrically-distributed magnetic torque profile as

$$\vec{\tau}(x) = A \cdot (\vec{M}(x) \times \vec{B}) = A \cdot M \cdot |\vec{B}| \cdot \sin \beta(x) \quad (2)$$

where A is the cross-sectional area of the swimmer (unit square meter), and β is the angle between the magnetic field \vec{B} and the local magnetic moment of the swimmer. Note that $\vec{\tau}(x)$ has a unit of Newton because it is a profile along the length. The swimmer deforms under the combined effect of $\vec{\tau}$ and the

interface constraints, i.e., water surface tension and buoyancy. The constraints counteract $\vec{\tau}$ and only allow the swimmer to deform slightly. The deformed shape of the swimmer varies with \vec{B} , as illustrated in **Fig. 1(c)**. When \vec{B} rotates around axis y , the swimmer shape changes correspondingly and forms a traveling wave like deformation along its body, generating propulsive forces to mobilize the swimmer into a bidirectional non-holonomic swimming gait, i.e., moving forward or backward but not sideward at an air-water interface. All on-water swimmers in this study have nominal dimensional values of $4.50 \times 1.50 \times 0.10 \text{ mm}^3$ or $2.00 \times 1.00 \times 0.03 \text{ mm}^3$ (length, width, and thickness).

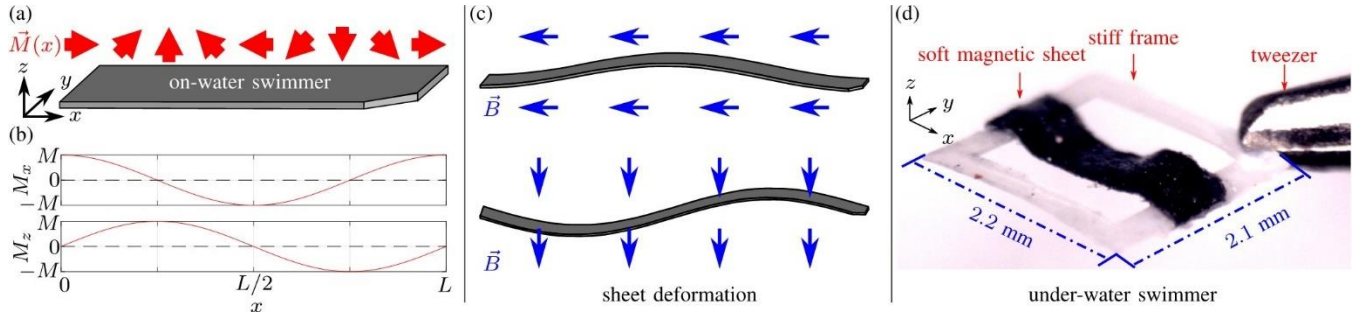


Fig. 1: Concepts of on-water and under-water swimmers. A sinusoidal magnetization profile $\vec{M}(x)$ is programmed into the soft magnetic composite sheet. A schematic of $\vec{M}(s)$ and its projections into axis x and z are plotted in (a) and (b), respectively. The on-water swimmer, i.e., a sheet constrained at an air-water interface, deforms once a magnetic field \vec{B} is applied, see (c). The deformation is exaggerated for better visualization. An under-water swimmer is shown in (d). See the Supplementary Information for details of the under-water swimmer frame.

2.2 Under-Water Swimmer

The surface tension is the dominant reactive force that determines an on-water swimmer shape at air-water interfaces. More importantly, the surface tension constrains the swimmer to the interface by preventing it from rolling or curling too much. Thus, the on-water swimmer stays at a horizontal plane and the applied magnetic field can be easily aligned with it to activate and control it. When the on-water swimmer is submerged in water and the surface tension is absent, it curls and rolls easily in the three-dimensional (3D) space, causing troubles in aligning the applied magnetic field with it. Even when this alignment is achieved, the swimmer deformation profiles in a rotating uniform magnetic field deviate from traveling wave shapes remarkably, deteriorating its swimming performance.

To achieve good under-water swimming, an under-water swimmer is formed by fixing the ends of an on-water swimmer on a stiff frame, which generates a fixed-fixed boundary condition for the central soft magnetic composite sheet. Although the fixed-fixed boundary condition is different with the one caused by the surface tension, it serves the same purpose and creates similar effects on constraining the soft sheet. A photograph of the under-water swimmer is shown in **Fig. 1(d)**. With this frame, the under-water swimmer does not curl and is less likely to roll in the 3D space. But, this frame also impedes the sheet deformation that is essential for the desired propulsion. Thus, the frame is configured to be slightly shorter than the sheet to alleviate this impediment. An approximate traveling wave like shapes are observed along the under-water swimmer sheet in the presence of a rotating uniform magnetic field. All under-water swimmers have nominal dimensional values of $2.2 \times 2.1 \times 0.03 \text{ mm}^3$.

2.3 Functional Soft Magnetic Composite Material for Swimming

The swimmers are made of a rectangular sheet of a soft magnetic composite and a stiff frame (only for under-water swimmers). The composite is formed by embedding permanent magnetic microparticles into elastomer matrices. These microparticles bear a programmed sinusoidal magnetization profile throughout the sheet and provide volumetrically-distributed torques in the presence of an externally-applied magnetic field. Under the combined effect of magnetic torques and the constraints provided by either surface tension and buoyancy forces or a stiff frame, the sheet deforms into traveling wave like shapes and interacts with the surrounding liquid to generate propulsive forces.

The fabrication of this soft magnetic composite sheet has three steps: defining geometries by photolithography (detailed in the Supplementary Information, **Fig. S1**), replica molding to obtain the sheet, and programming the magnetization profile. An elastic polymer (Ecoflex 0050, Smooth-On) was uniformly mixed with permanent magnetic microparticles (MQFP-15-7, NdPrFeB, Magnequench) at 1:1 mass ratio. This mass ratio provides a good balance between the magnetization strength and the material stiffness. This magnetic slurry was then poured into a negative sheet mold. A razor blade scraped away excess materials. This polymeric mixture cured inside the mold, forming the desired soft magnetic composite sheet. The cured sheet was taken out from the mold manually using a tweezer, wrapped around a cylindrical wire, and magnetized in a uniform magnetic field of 1.1 T created by two permanent magnets (1 inch cube, NdFeB, N40, Magnet4US). The last step programmed a sinusoidal magnetization profile $\vec{M}(s)$ throughout the sheet, enabling it to deform into undulatory motions in a rotating uniform magnetic field. This fabrication process is illustrated in **Fig. 2**. The sheet has a simple structure and is made of homogeneous materials, making itself easy and cost-effective to fabricate. Without any complicated body structures or patterns, the swimmers should also be convenient to fabricate on the micron scale. An under-water swimmer needs an additional stiff frame. An ultra-low viscosity casting resins (Smooth-Cast 310, Smooth-On) was poured into the negative mold and excess resins were scraped off by a razor blade, see **Fig. 2(d)**. The resins cured into a single piece of stiff solid frame, which was taken out manually using tweezers. In the last step, the magnetized sheet was manually glued to the frame with an initial curvature using the liquid plastic (Smooth-Cast 310, Smooth-On), see **Fig. 2(f)**.

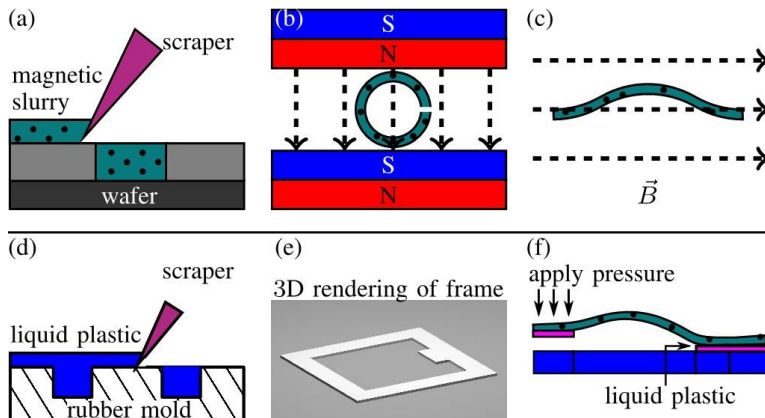


Fig. 2: Fabrication of the soft magnetic composite sheet and the stiff frame. The mixture of a polymer and permanent magnetic particles were poured into the sheet mold, and scraped by a razor blade in (a). After curing, the sheet was magnetized in (b) to program a sinusoidal magnetization profile into its body. As a result, the sheet deforms in an applied magnetic field \vec{B} , see (c). A liquid plastic was poured into the soft rubber mold for the frame, and scraped to remove the excess amount, see (d). The plastic cured into the stiff frame, whose rendering is shown in (e). The two ends of the soft magnetic sheet were dipped in the liquid plastic and pressed on the frame to attach itself.

To verify the resultant magnetization profile $\vec{M}(s)$ along the sheet is indeed a sinusoidal shape, the magnetized sheet was placed on a sensor (cmos-magview S, Matesy GmbH - Magnetic Technologies

and Systems) that measures the normal component of a magnetic field. The measurement was then compared with the predictions made by a magnetic dipole-based model using a custom script developed on Matlab. The two sets of data show a convincing similarity with each other, proving that a sinusoidal magnetization profile $\vec{M}(s)$ was created as expected. The results of this verification are presented in Fig. 3.

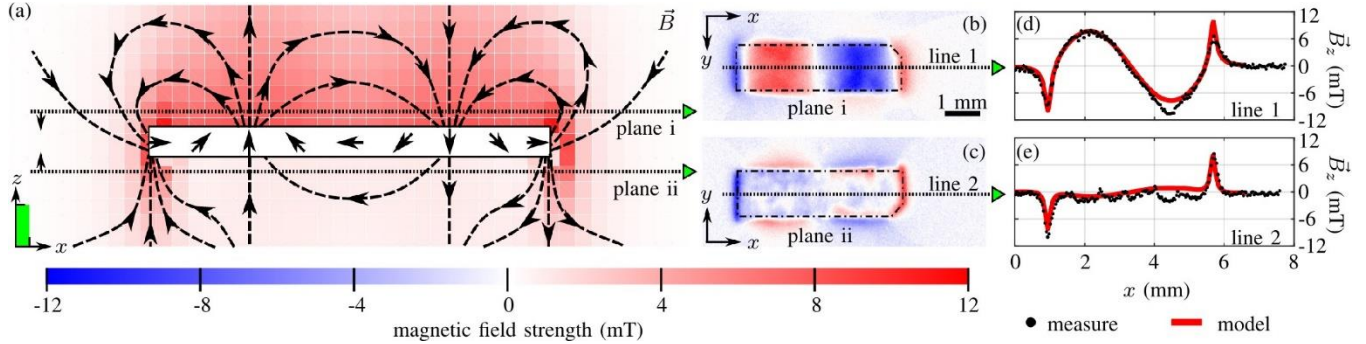


Fig. 3: Measurement and prediction of the magnetic field near the magnetized sheet. The magnetic field on the middle x - z plane of the sheet is simulated and its magnitude is color coded in (a). The magnetic field lines are plotted qualitatively. The green rectangle represents a square of 0.15 mm in size. Note the scales for axis x and y are different for better visibility. Measurements were taken at plane i and ii and shown in (b) and (c), respectively. Data on line 1 and 2 are compared with simulation results in (d) and (e), respectively.

3 Results and discussions

3.1 On-Water Swimming

This subsection models the swimmer shapes and characterizes the swimming performance in one of its working scenarios, i.e., on-water swimming. An autonomous path-following experiment is presented to demonstrate the maneuverability of on-water swimmers.

3.1.1 Force Analysis and Swimmer Shape Model

Here, the shape of an on-water swimmer in uniform magnetic fields is modeled based on the Euler-Bernoulli beam theory from underlying physical principles. With all pertinent parameters measured independently, the predicted shapes in varying magnetic fields show a favorable agreement with the corresponding experimental observations.

When a magnetic field is absent, a swimmer (length L , width W , and thickness T) at an air-water interface experiences gravity, buoyancy, and surface tension. At this state, the swimmer exhibits negligible deformation due to its low gravity and density values. Thus, it is assumed without much loss of accuracy that the swimmer has zero gravity, and it remains flat and does not disturb the air-water interface when no magnetic field is applied. Applying a magnetic field \vec{B} causes a magnetic torque profile $\vec{\tau}(x)$ that is described by Eq. (2) and the swimmer deforms as a result. Since the swimmer rests on the air-water interface, its deformation interferes with the water surface and causes the surface tension \vec{F}_t and the buoyancy \vec{F}_b on it to change correspondingly. Moreover, the relative angle β between

$\vec{M}(x)$ and \vec{B} changes as the swimmer deforms. Thus, the swimmer deformation converges to a shape that balances the internal shear forces and the external forces and torques.

As a convention, the positive direction of torques and forces are defined to be counterclockwise (from $+x$ to $+z$) and upward ($+z$), respectively. The swimmer does not deform along its width, i.e., axis y , and its shape is fully described by a shape profile $\omega(s)$ ($s \in [0, L]$) in the x - z plane. The value of $\omega(s)$ is obtained by subtracting the height of the undisturbed water surface from the height of the swimmer bottom surface. The coordinate s is defined along the swimmer body and coincides with axis x when the swimmer is undeformed.

The forces and torques on the swimmer are schematically illustrated in **Fig. 4**. Within the scenario discussed here, the swimmer deformation ω is always smaller than one tenth of its length L . Thus, the buoyancy \vec{F}_b is considered to be always along axis z and its distribution $\vec{F}_b(s)$ with a unit of Newton per meter is calculated by

$$\vec{F}_b(s) = \rho g W \cdot \omega(s) \quad (3)$$

where ρ is the water density (1000 kg/m^3), g is the gravitational acceleration constant (9.8 m/s^2), and W is the swimmer width in meter. The surface tension \vec{F}_t exists at the boundary of the contact area between the swimmer and the water. The direction of \vec{F}_t is along the disturbed water surface and perpendicular to the boundary, forming an angle θ_t with the horizontal plane. The \vec{F}_t along the swimmer length and width are denoted by $\vec{F}_{t, \text{len}}$ and $\vec{F}_{t, \text{wid}}$, respectively. The horizontal component of $\vec{F}_{t, \text{len}}$ points along axis y and does not affect the swimmer shape ω in the x - z plane. The vertical component of $\vec{F}_{t, \text{len}}$, i.e., $\vec{F}_{t, \text{len}, v}$, and $\vec{F}_{t, \text{wid}}$ are relevant with ω and computed correspondingly as

$$F_{t, \text{len}, v}(s) \Big|_{s \in [0, L]} = 2\gamma \sin \theta_t(s) \quad (4)$$

$$F_{t, \text{wid}, v}(s) \Big|_{s \in [0, L]} = \gamma W \sin \theta_t(s) \quad (5)$$

and

$$F_{t, \text{wid}, h}(s) \Big|_{s \in [0, L]} = \gamma W \cos \theta_t(s) \quad (6)$$

respectively. The constant γ is the surface tension coefficient (0.072 N/m for an air-water interface). The force profile $F_{t, \text{len}, v}(s)$ has a coefficient of 2 because both long edges of the swimmer experience the surface tension forces with the same vertical components. Note that $F_{t, \text{len}, v}(s)$ has a unit of Newton per meter while $F_{t, \text{wid}, v}(s)$ and $F_{t, \text{wid}, h}(s)$ have a unit of Newton. This difference is because $F_{t, \text{len}, v}(s)$ is a force profile but $F_{t, \text{wid}, v}(s)$ and $F_{t, \text{wid}, h}(s)$ are force components.

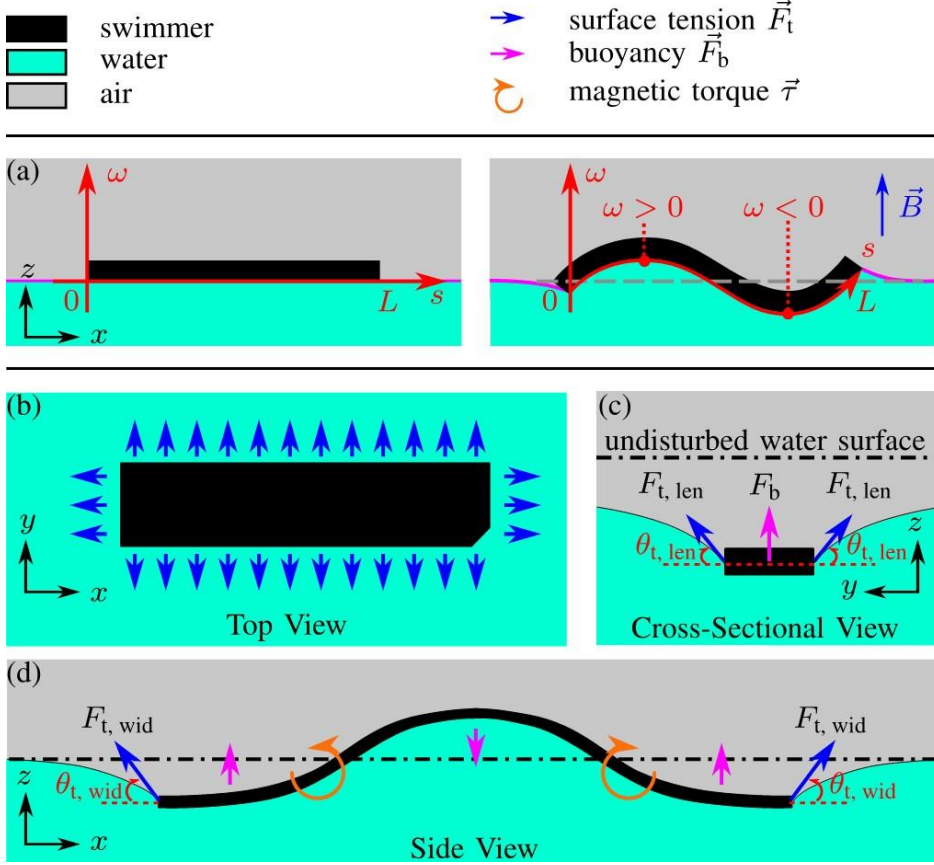


Fig. 4: On-water swimmer shape definition and the forces and torques it experiences. The swimmer shape is described by ω and defined in (a). The swimmer deforms when a magnetic field is applied and interacts with the water surface. The forces and torques applied on the swimmer when it deforms are qualitatively drawn in the top view, cross-sectional view, and side view in (b), (c), and (d), respectively. The surface tension applied along the swimmer length is not shown in (d) for better visibility. The arrow sizes do not represent the corresponding force magnitudes.

The total bending moment $Q(s)$ on the swimmer body is

$$Q(s) = Q_{\tau}(s) + Q_b(s) + Q_t(s) \quad (7)$$

where $Q_{\tau}(s)$, $Q_t(s)$ and $Q_b(s)$ are the bending moment caused by the magnetic torque $\vec{\tau}$, surface tension \vec{F}_t , and buoyancy \vec{F}_b , respectively, and they can be calculated using the relationship between the load, shear force, and bending moment on a beam. The bending moment Q_{τ} and Q_b are computed as

$$Q_{\tau}(s) = - \int_0^s \tau(\tilde{s}) d\tilde{s} \quad (8)$$

and

$$Q_b(s) = \int_0^s F_b(\tilde{s}) \cdot (s - \tilde{s}) d\tilde{s} \quad (9)$$

respectively. The dummy variable \tilde{s} is a placeholder and disappears completely in final results. The bending moment Q_t is further divided into

$$Q_t(s) = Q_{t, len, v}(s) + Q_{t, wid, v}(s) + Q_{t, wid, h}(s) \quad (10)$$

where $Q_{t, len, v}$, $Q_{t, wid, v}$, and $Q_{t, wid, h}$ are caused by $F_{t, len, v}$, $F_{t, wid, v}$, and $F_{t, wid, h}$, respectively. The expressions for these terms are

$$Q_{t, len, v}(s) = \int_0^s F_{t, len, v}(\tilde{s}) \cdot (s - \tilde{s}) d\tilde{s} \quad (11)$$

$$Q_{t, wid, v}(s) = F_{t, wid, v} \cdot s \quad (12)$$

and

$$Q_{t, wid, h} = F_{t, wid, h} \cdot (\omega(s) - \omega(0)) \quad (13)$$

As mentioned before, the swimmer deformation ω is always smaller than one tenth of its length L , satisfying the ‘small deformation’ assumption of the Euler-Bernoulli beam theory. Thus, the curvature κ of the swimmer body is related to its bending moment Q using the Euler-Bernoulli beam theory as

$$\kappa(s) = Q(s) \cdot (EI)^{-1} \quad (14)$$

where E and $I = WT^3/12$ are the Young's modulus and the second moment of area of the swimmer sheet, respectively. Finally, the swimmer shape profile $\omega(s)$ can be derived from its curvature profile $\kappa(s)$.

3.1.2 Parameter Measurement

The parameters relevant to the proposed swimmer shape model were measured independently, to theoretically predict the swimmer shapes from underlying physical principles and verify the model efficacy by comparing predictions against observations. This specific swimmer had dimensional values of $4.47 \times 1.33 \times 0.109 \text{ mm}^3$ (length, width, and thickness). The length and width were measured using a caliper (Starrett, resolution 0.01 mm) and the thickness was measured by a micrometer (Mitutoyo, resolution 0.001 mm). The applied magnetic field in the shape observation experiment had a strength of 10 mT, which was verified by a gaussmeter (Model 425, LakeShore).

The swimmer magnetization could not be measured directly because its direction varied along the body. Thus, eight cubes with a side length of 3.1 mm were made of the soft magnetic composite that was used by the swimmer. These cubes were magnetized in the same magnetizing setup with the swimmer, and then glued into a larger cube that exhibits a stronger overall magnetic moment. The magnetic field of the larger cube was measured using the gaussmeter at several known distances from the cube. The obtained data was fitted to a magnetic dipole model to estimate the magnetic moment. A magnetization value was obtained by dividing the magnetic moment by the total volume of the cube. The obtained magnetization value of the cube was assumed to be identical with the swimmer magnetization, because they shared the same material and went through the same magnetization process. The magnitude of magnetization of the soft magnetic composite was measured to be 45 kA/m.

Another parameter that needed to be measured is the Young's modulus E of the sheet. In the measurement, a sheet was fixed by one end and leaving the other one free. A micro-force sensing probe (FT-S100 probe, FemtoTools) applied a point force on the sheet to bend it, mimicking the sheet deformation when it swims. The value of $E = 0.165 \text{ MPa}$ was derived from the recorded values of the force amplitude and corresponding deformation. More details about this measurement can be found in the Supplementary Information.

3.1.3 Numerical Simulation of Swimmer Shapes

With the proposed shape model and the measured parameter values, there is only one problem left to be addressed before the swimmer shape can be simulated from first principles: The swimmer has sharp edges, whose interaction with the water surface is complex and hinders the analysis of the surface tension \vec{F}_t (**Fig. 5(a)**). A vertical swimmer edge is described as a combination of a straight line segment and two quadrants (radius $r \geq 0$) at both ends. When the water-air-swimmer (WAS) intersection is within the quadrant region, the surface tension angle θ_t is related to the contact angle θ_c and the submerge angle δ as $\theta_t = \theta_c + \delta - \pi$. The value of θ_t increases with δ as the swimmer goes further

down into the water until the WAS intersection moves into the line segment region, where θ_t is constant and $\theta_t = \theta_c - \pi/2$. Since the swimmer thickness T is small compared with its other dimensions and deformation magnitude, the thickness T is neglected in the calculation of the swimmer shape ω and the swimmer edge is approximated as a hemisphere with infinitesimal radius, i.e., $r \rightarrow 0$. As a result, the value of θ_t varies with ω , while the WAS intersection remains at the same spot on the swimmer.

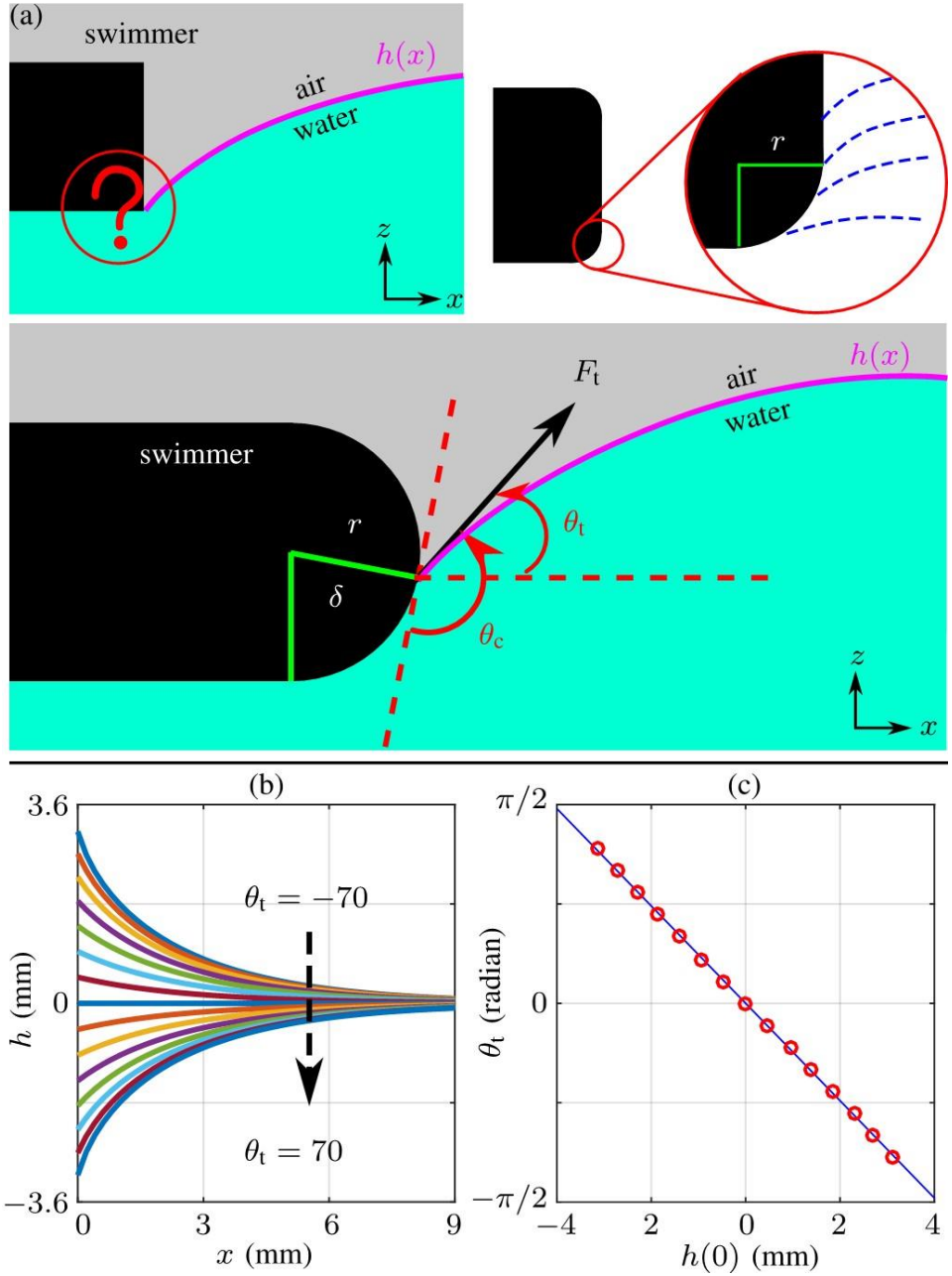


Fig. 5: The sharp edge problem of the swimmer and its treatment. A sharp swimmer edge is represented by the combination of a line segment and two quadrants with radius r . When its thickness is ignored, the swimmer edge is approximated as a hemisphere, see (a). The dashed curves represent the different water surface profiles for varying intersection locations. Different water surface profiles h are plotted in (b) when the surface tension angle θ_t at the swimmer edge varies. The values of θ_t are shown in (c) with respect to different swimmer edge positions.

An air-water interface disturbed by a hemisphere has been described by Song et al.³⁹ based on the Young-Laplace equation as

$$\rho gh(x) = \gamma \cdot \left(\frac{\frac{d^2}{dx^2} h(x)}{\left(1 + \left(\frac{d}{dx} h(x)\right)^2\right)^{1.5}} \right) \quad (15)$$

where $h(x)$ is the air-water interface profile and other symbols have already been defined. Their work assumed that the cylinder is infinitely long, which is not true for the swimmer and may potentially impair the simulation accuracy using **Eq. (15)**. Taking the WAS intersection as the origin of axis x , the boundary conditions for **Eq. (15)** are $dh(0)/dx = \tan \theta_t$, $h(\infty) = 0$, and $dh(\infty)/dx = 0$. As suggested by Song et al.,³⁹ only the first two boundary conditions are used in the numerical calculation of h , whose result will automatically satisfy the last condition. In addition, $h(\infty)$ is evaluated at $x = 0.02$ m to approximate the case at $x = \infty$. Numerically solving **Eq. (15)** using Matlab, the water surface profile h is obtained for different surface tension angles θ_t , see **Fig. 5(b)**. The value of θ_t is plotted against the depth of the WAS intersection $h(0)$ in **Fig. 5(c)**. A least-squares regression of the data yields the following relationship with a coefficient of determination of 0.9994:

$$\theta_t = 7.652 \times 10^{-6} - 3.847 \times 10^2 h(0) \quad (16)$$

At any specific boundary point of the swimmer, the swimmer deformation equals the WAS interaction depth, i.e., $\omega(s) = h(0)$. Therefore, the one-to-one mapping between $h(0)$ and θ_t built by **Eq. (16)** enables the calculation of $F_{t, \text{len. v}}(s)$, $F_{t, \text{wid. v}}(s)$, and $F_{t, \text{wid. h}}(s)$ when $\omega(s)$ is known. Note that the contact angle θ_c is not involved in this calculation process. The contact angle θ_c only affected the position of the WAS intersection on the swimmer edge, which was irrelevant since the swimmer thickness T has been ignored.

Since the forces and torques on the swimmer vary with the swimmer shape ω , ω cannot be analytically solved and its value can only be obtained by iterative numerical calculations until a convergence is achieved. Thus, an iterative numerical algorithm was built using Matlab to predict ω in various magnetic fields from first principles. The algorithm consists of the following steps. (1). Initialize the simulation: define the simulation points along the swimmer, the iteration step size, and the convergence tolerance. (2). Gather the known parameters: specify the swimmer dimension values, the magnetization, the Young's modulus, and the strength and direction of the applied magnetic field. (3). Calculate the forces and torques on the swimmer using the swimmer current shape ω_{cur} and **Eq. (2-6)**. (4). Obtain the swimmer curvature κ using **Eq. (7-14)**. (5). Divide the variation in κ by the iteration step size and then use it to get the swimmer new shape ω_{new} . (6). Calculate the forces and torques on the swimmer, excluding magnetic torques, using ω_{new} , and then rotate and/or vertically move ω_{new} until the forces and torques balance each other. (7). Set $\omega_{\text{cur}} = \omega_{\text{new}}$, and repeat step (3-7) until the change in ω between iterations is smaller than the convergence tolerance. A pseudocode is provided in the Supplementary Information to further explain the algorithm.

3.1.4 Experimental Swimmer Shape Observations

This specific swimmer was placed at an air-water interface within a uniform magnetic field, which was created by a custom-built two-dimensional (2D) electromagnetic coil system (**Fig. 6(a)**). The field direction was varied to form different angles with the length of the swimmer in the same plane. In each case, the swimmer shape was observed and compared against the corresponding theoretical prediction, to evaluate the efficacy of the proposed model and simulation algorithm. Once applied, the magnetic

field rotated the swimmer horizontally to a certain orientation, because the swimmer has a nonzero net magnetic moment. A camera (IL3, Fastec Imaging) mounted at a tilting angle $\phi = 43^\circ$ captured this rotation at 1000 frames per second. The swimmer shape was extracted from the frame in which the swimmer length was coplanar with the magnetic field. If the camera observed the swimmer from a side-view perspective without tilting, the part of swimmer that deformed downwards would be blocked by the water surface and therefore its deformation profile could not be accurately extracted. The tilted camera could record the complete swimmer shape without interference. However, the extracted swimmer shapes were distorted by the tilting angle, see **Fig. 6(b)**. This distorted swimmer shape profile was corrected as $\omega_{\text{cor}}(s) = \omega_{\text{obs}}(s)/\cos \phi$.

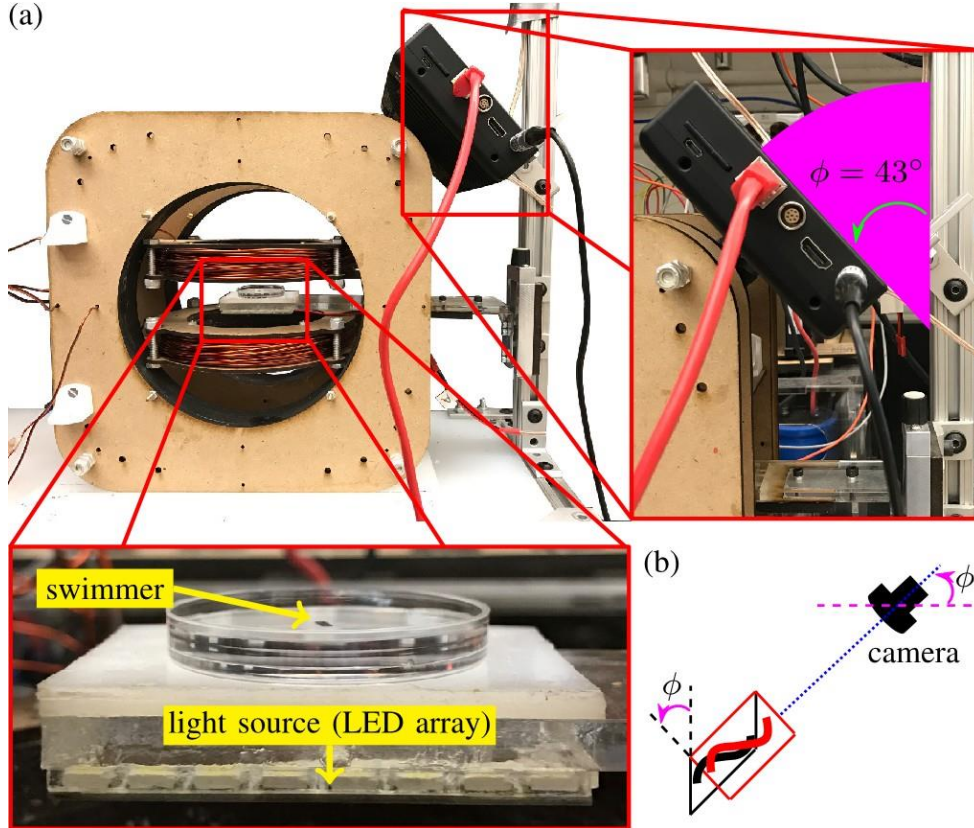


Fig. 6: The setup and schematics for observing the on-water swimmer shape. The 2D coil system and the camera are shown in (a). The insets show the camera tilting angle and swimmer sample at the center of the coil system. The image captured by the camera is distorted by the tilting angle, see (b).

The angle between the swimmer and the applied magnetic field varied from 0° to 315° at an interval of 45° . Frames showing the swimmer in the magnetic field with different directions are presented in **Fig. 7**. The corrected swimmer shape profiles $\omega_{\text{cor}}(s)$ are plotted together with the theoretical predictions beneath corresponding frames. Since the swimmer was observed from a tilting angle, the water surface filled the whole field of view as a plane, instead of a line when it was observed from the side. As a result, the height of the swimmer with respect to the undisturbed water surface could not be determined. To enable the swimmer shape comparison, the average vertical position of each $\omega_{\text{cor}}(s)$ was adjusted to match the average of its corresponding predicted profile. Then the root-mean-square-deviation (RMSD) between the two profiles were calculated and given in each frame. The average RMSD value, i.e., $46.3 \mu\text{m}$, is only 1% of the magnitude of the swimmer length, i.e., 4.47 mm , and about 10% of the swimmer peak-to-peak deformation, which is around $500 \mu\text{m}$. The low values of the RMSD suggest a good agreement between the theoretical predictions and the experimental observations of the swimmer

shape, which further endorse the efficacy of the proposed model and simulation algorithm. These nonzero RMSD values could be ascribed to the ignorance of the swimmer thickness T , the aberration in using Eq. (15) while the swimmer is not infinitely long, and the tolerances in parameter measurements.

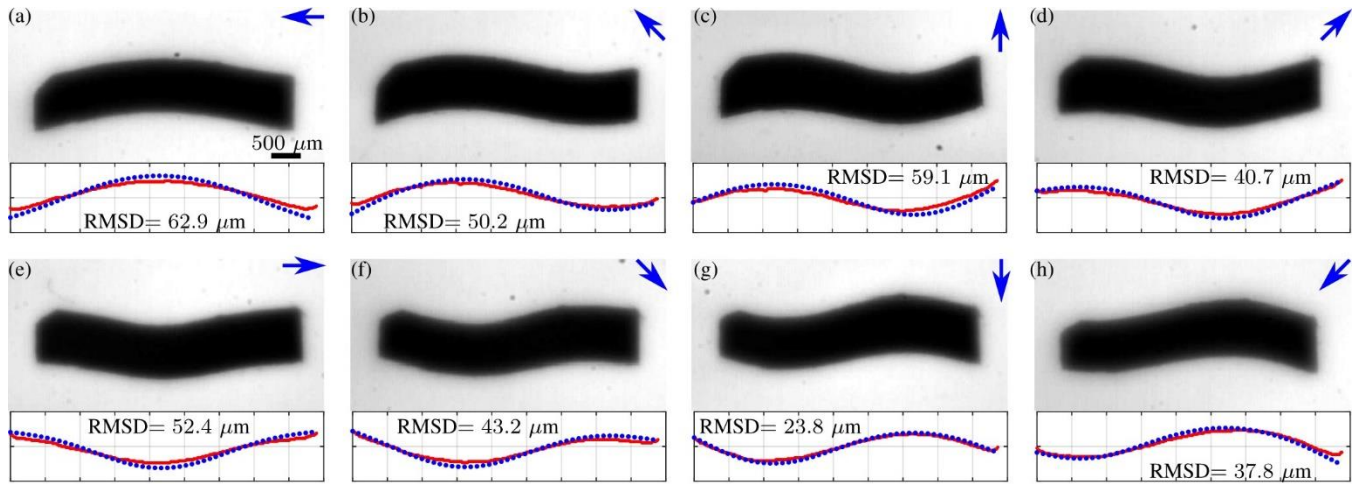


Fig. 7: A comparison between experimental and theoretical swimmer shapes in a magnetic field with varying directions. Dots represent the experimental swimmer shape ω_{cor} , which was automatically extracted from captured frames and corrected by the tilting angle ϕ using a Matlab script. Curves show the predicted swimmer shapes. The arrows denote the directions of the applied 10 mT magnetic field. The RMSD value is given, which stands for the root-mean-square-deviation between the theoretical and the experimental swimmer shapes. Each tick of the abscissa and ordinate is 500 μm .

3.1.5 Swimming Demonstration and Characterization

When an on-water swimmer receives a rotating uniform magnetic field, i.e., the actuation field \vec{B}_a , in its x - z plane, it deforms into traveling wave like profiles and swims along its axis x . As discussed in our previous work,^{12,13} a small steering magnetic field \vec{B}_s in the x - y plane needs to be applied along the swimmer net magnetic moment to ensure that \vec{B}_a remains in the x - z plane of the swimmer. The addition of \vec{B}_s shifts the overall magnetic field, making its component along one direction larger than the ones along other directions. Consequently, the swimmer experiences a net torque over time that aligns the swimmer with the designated direction. Without \vec{B}_s , there are torques with equal amplitudes that try to align the swimmer with opposite directions, causing the swimmer to oscillate or even rotate with uncontrolled moving direction.

Using two fields requires a 3D electromagnetic coil system, whose workspace can only be observed from its top or side. A video of an on-water swimmer swimming within the 3D coil system is shown in **Movie 1**. The swimmer profiles cannot be extracted accurately from sideview observations.

To clearly measure the swimmer deformation while it swims, an on-water swimmer was re-magnetized slightly by moving a permanent magnet close to it, to obtain a net magnetic moment along its axis x . In this way, \vec{B}_s is coplanar with \vec{B}_a and can be generated by the 2D coil system in **Fig. 6**. More details about how the two magnetic fields cooperate to propel and directionally control the swimmer can be found in our previous work.¹²

The swimmer was placed at an air-water interface and activated by \vec{B}_a of 9 mT rotating at 40 Hz, while

\vec{B}_s is along the swimmer length (axis x) with a magnitude of 2 mT. The swimmer was filmed at 800 Hz using the setup shown in **Fig. 6** with a camera tilting angle $\phi = 45^\circ$, and the video is shown in **Movie 2**. A quantification of the similarity between the swimmer deformation and a traveling sinusoidal wave (TSW) provides a useful index for comparing the swimming performance of different swimmers in various scenarios.

First, the traveling wave component (TWC) of the swimmer deformation was obtained in following steps. The swimmer shape profile $\omega(s)$ was extracted from captured frames and corrected by the tilting angle. Then, it was decomposed into a Fourier series and only the first order terms were kept as

$$\omega(s) \approx C + a \cos(2\pi s \cdot L^{-1}) + b \sin(2\pi s \cdot L^{-1}) \quad (17)$$

where C is a constant, and a and b are the first-order Fourier coefficients. The standard expression of a TSW is

$$\tilde{\omega}(s) = \tilde{R} \sin\left(\frac{2\pi s}{L} + \tilde{\varphi}(t)\right) = \tilde{R} \left(\cos\frac{2\pi s}{L} \sin\tilde{\varphi}(t) + \sin\frac{2\pi s}{L} \cos\tilde{\varphi}(t) \right) \quad (18)$$

where $\tilde{\omega}(s)$ is the displacement, \tilde{R} is the magnitude, and $\tilde{\varphi} = (-\pi, \pi]$ is the phase angle. Equating **Eq. (17)** and **(18)** derives that $a = \tilde{R} \sin \tilde{\varphi}$ and $b = \tilde{R} \cos \tilde{\varphi}$. Thus, the amplitude and phase angle of the TWC are

$$R = \sqrt{a^2 + b^2} \quad (19)$$

and

$$\varphi = \tan^{-1}(a \cdot b^{-1}) \quad (20)$$

respectively. Thus, the amplitude R and phase angle φ of the TWC in a swimmer profile $\omega(s)$ can be obtained using **Eq. (17)**, **(19)** and **(20)**. The obtained R and φ from 10 frames in one rotation of \vec{B}_a are plotted in a polar coordinate frame in **Fig. 8(a)**. Each data point represents a TWC vector with the information of an amplitude R and a phase angle φ .

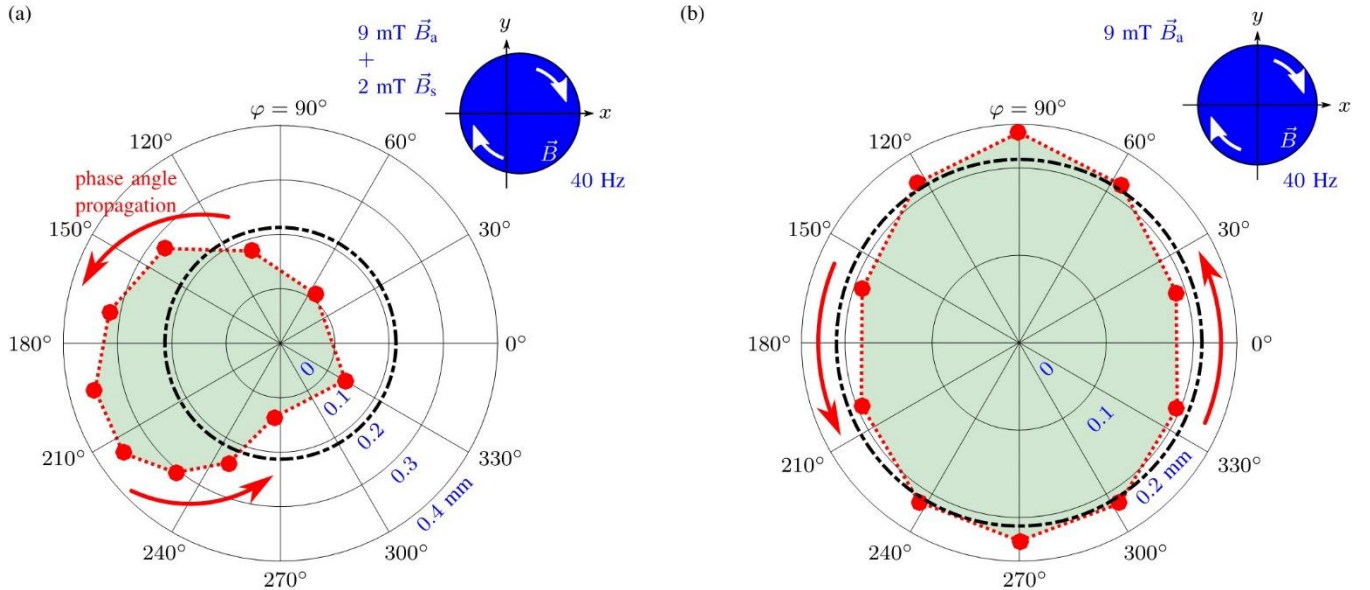


Fig. 8: Results of the TWC analysis of an on-water swimmer. The swimmer has dimensional values of $4.59 \times 1.31 \times 0.106 \text{ mm}^3$, and was activated by a uniform magnetic field of 9 mT rotating at 40 Hz. A 2 mT steering field was added to maintain the swimmer orientation, causing the overall field to shift, as shown by the solid circle in (a). The TWC vectors extracted from observed swimmer profiles are plotted in (a). The dashed circle is the equivalent circle. The corresponding theoretical results of the swimmer in the same rotating uniform magnetic field with no steering field are plotted in (b).

Rotate all these TWC vectors in the polar coordinate frame along the phase propagation direction, i.e., counter-clockwise, until they meet their immediate following vectors. The area swept by these TWC vectors is

$$S_{\text{swp}} = \sum_1^{10} \left(\pi R_i^2 \cdot \frac{\Delta\varphi_i}{2\pi} \right) \quad (21)$$

where $\Delta\varphi_i \in (0, \pi)$ is the phase angle difference between TWC vector $i + 1$ and i . When $i = 10$, $\Delta\varphi_i$ is calculated between TWC vector 1 (the first one) and 10 (the last one). Note that S_{swp} is not the gray region in **Fig. 8**. A circle with its area equal to S_{swp} is named as the equivalent circle. The radius length of the equivalent circle represents the swimming amplitude, meaning that a TSW with the same swimming amplitude will lie exactly on the equivalent circle in the polar coordinate frame. To compensate the swimming magnitude variation between swimmers of different length, the equivalent circle radius is normalized with respect to the swimmer length L , resulting in a variable named the normalized swimming amplitude R_{nor} as

$$R_{\text{nor}} = \sqrt{S_{\text{swp}} \cdot \pi^{-1} \cdot L^{-1}} \quad (22)$$

A large R_{nor} value means big swimming deformation magnitude that causes strong propulsive forces.

As mentioned before, a TSW with the same swimming amplitude exactly fills the equivalent circle. Thus, the overlapped area between the region swept by the TWC vectors and the equivalent circle describes the spatial difference between the swimmer deformation and a TSW. This area is referred to as S_{ovlp} and normalized with respect to S_{swp} , resulting in a variable named as the circularity ϵ that is computed as

$$\epsilon = S_{\text{ovlp}} \cdot S_{\text{swp}}^{-1} \quad (23)$$

The phase angle of a TSW changes at a constant rate. Taking ten measurements within each \vec{B}_a rotation period, the phase angle difference between two measurements of a TSW is $\pi/5$ and has zero variation. The standard deviation of the experimental phase angle differences $\Delta\varphi_i$ was calculated and normalized to characterize the temporal difference between the swimmer deformation and a TSW. The normalized standard deviation is named as the temporal uniformity ψ and computed as

$$\psi = \sqrt{\frac{1}{9} \sum_1^{10} \left| \Delta\varphi_i - \frac{\pi}{5} \right|^2} \cdot \frac{5}{\pi} \quad (24)$$

The average of the experimental $\Delta\varphi_i$ is also $\pi/5$ because each cycle of magnetic field rotation corresponds to 10 frames.

The values of these characterization parameters obtained from this experiment are summarized in Table 1. The R_{nor} represents the general strength of the TWC in the swimmer deformation. The values of ϵ and ψ describe the spatiotemporal similarity between the swimmer deformation and a TSW. Note that the swimmer magnetization profile was distorted in the re-magnetization process and the applied magnetic field is shifted due to the addition of \vec{B}_s . If these two unideal factors are ruled out, the deformation profiles of an on-water swimmer with a sinusoidal magnetization profile activated in a \vec{B}_a of 9 mT rotating at 40 Hz were predicted and analyzed using the aforementioned steps. The TWC vectors of the swimmer in this case are plotted in **Fig. 8(b)**. The resultant characterization parameter

values are summarized in **Table 1** and show that the swimmer swims better if the distortions in its magnetization and the overall applied magnetic field are removed.

Table 1: Traveling wave component (TWC) analysis results of on-water and under-water swimming

setting			R_{nor}	ϵ	ψ
name	scenario	mode			
traveling sinusoidal wave	n.a.	n.a.	n.a.	1	0
onwater swimmer	water surface	sim.	0.047	0.932	0.093
onwater swimmer	water surface	exp.	0.046	0.622	0.655
onwater swimmer	under water	sim.	0.087	0.744	1.035
underwater swimmer	under water	exp.	0.075	0.937	0.781

3.1.6 Feedback Controller

An on-water swimmer was placed at an air-water interface and controlled by the superposition of \vec{B}_a and \vec{B}_s , which were generated by the 3D coil system proposed in our previous work.¹² Based on the waypoint-following controller that has been proposed in our previous work, a more advanced computer vision-based proportional feedback controller was devised with similar working principles. The closed-loop controller manipulated the swimmer to perform path-following tasks: The swimmer autonomously followed six segments of paths that formed the letters ‘UT’, see **Fig. 9**. The controller changed the output magnetic field continuously to create the rotating \vec{B}_a and constant \vec{B}_s , while the swimmer position was extracted from the live images fed by the optical camera at 60 Hz. Based on the feedback information, the controller modifies, also at 60 Hz, the amplitudes and directions of \vec{B}_a and \vec{B}_s to change the swimming speed and direction of the swimmer. The clear speed control and small path deviations in **Fig. 9(b)** and **(c)** demonstrate the good dexterity and maneuverability of the on-water swimmer at an air-water interface, which can be used to position floating objects. This trial is also shown in **Movie 3**.

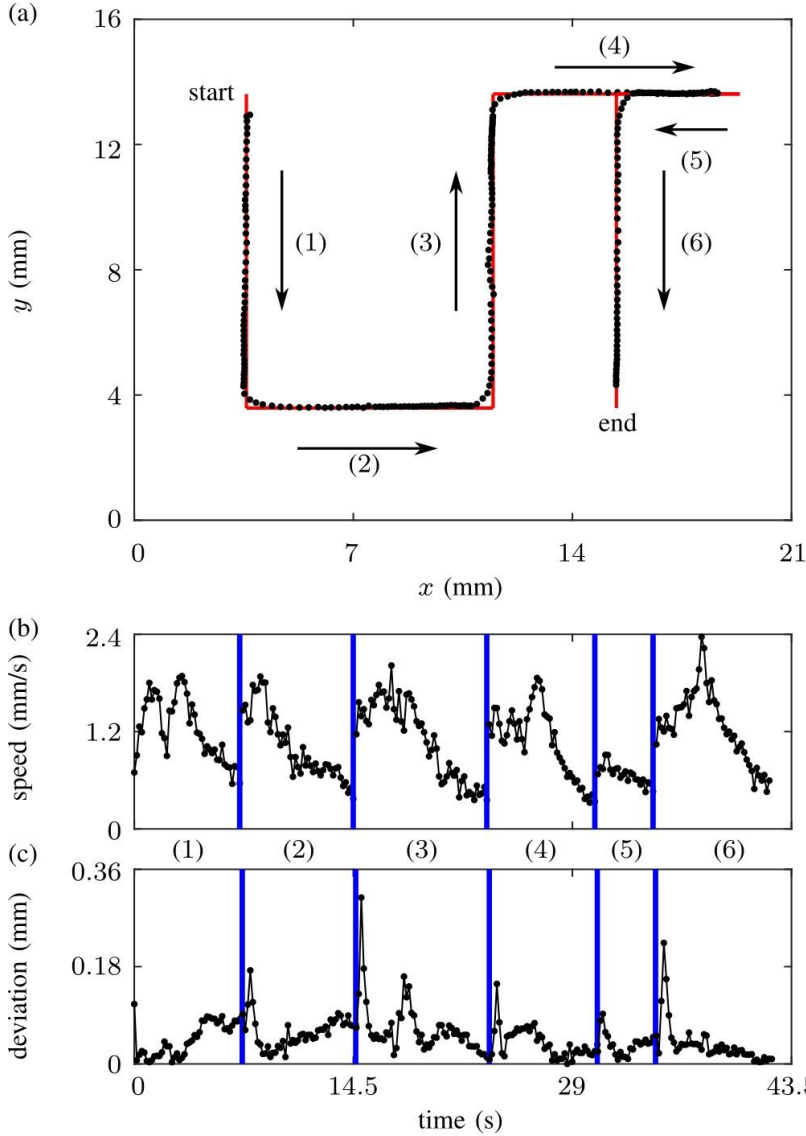


Fig. 9: The path-following results of an on-water swimmer ($1.85 \times 0.85 \times 0.038 \text{ mm}^3$) at an air-water interface actuated by a rotating magnetic field (10 mT, 40 Hz) and a steering field (2 mT). The swimmer centroid positions are plotted by the dots in (a), while the lines mark the specified paths. The swimmer speed and its deviation from the desired paths are plotted in (b) and (c), respectively. The dashed lines divide the data into each path segment. This trial is also shown in **Movie 3**.

3.2 Under-Water Swimming

This subsection discusses the undulatory deformation of the soft magnetic composite sheet when it is submerged under water. Being able to generate propulsive forces in water widely extends the range of potential applications of a microrobotic device, enabling it to work in tasks such as drug transportation⁴⁰ and minimally invasive surgery⁴¹. Previously, we have shown that an on-water swimmer moved on a horizontal under-water surface.¹² However, once the swimmer was away from the surface, it would easily curl and then roll with the rotating magnetic field with no net movement. Here, we build an under-water swimmer with an additional stiff frame, which exhibits ameliorated performance.

3.2.1 On-Water Swimmer Submerged in Water

The shapes of an on-water swimmer submerged in water were predicted by the proposed numerical

algorithm and shown in **Fig. 10(a)**. In this case, the surface tension and buoyancy forces were removed from the simulation, leaving the magnetic torques as the sole factor that deforms the swimmer. Since the swimmer curls much easier in water without surface tension, the magnetic field strength in the simulations was set to be 0.4 mT and is only 4.4% of the strength used to activate a swimmer at an air-water interface, i.e., 9 mT. The swimmer was initially flat and then deformed by a constant magnetic field at various directions. This simulated case was different with applying a rotating magnetic field, in which case the swimmer was highly likely to curls and then rolls with the field with no further shape change or net movement.

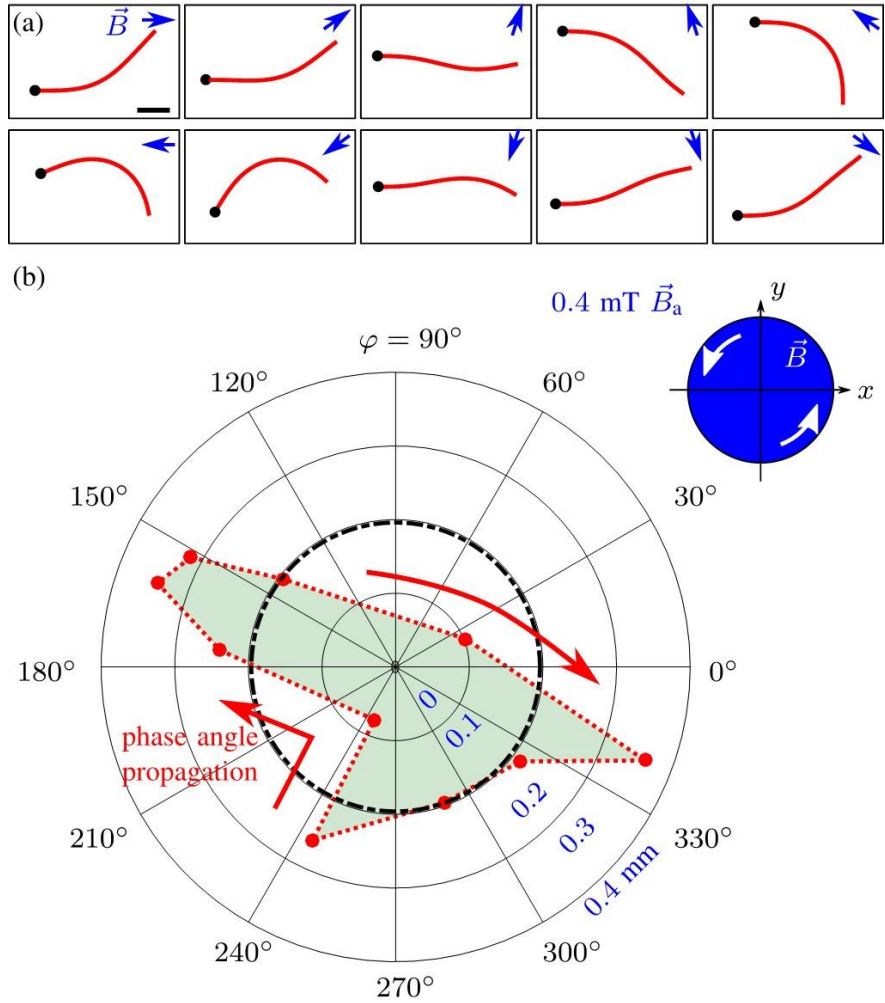


Fig. 10: Simulated shapes and the corresponding TWC analysis results of an on-water swimmer in constant magnetic fields of 0.4 mT when the swimmer is submerged in water. The swimmer is $2.20 \times 0.66 \times 0.03 \text{ mm}^3$ large. The predicted swimmer shapes in various field directions are shown in (a), where the dot marks the left end of the swimmer. The TWC analysis results are plotted in (b), where the dashed circle is the equivalent circle.

The TWC analysis was performed on the swimmer shapes in this ‘idealized’ case that assumed perfect alignment with magnetic fields and no rolling in circles. The analysis results are plotted in **Fig. 10(b)** and summarized in **Table 1**. The result clearly shows that the on-water swimmer submerged in water does not approximate a TSW very well, which is also endorsed by the values of ϵ and ψ . The deviation of the shape of an on-water swimmer submerged in water from a TSW could potentially explain the observed inferior swimming performance: The on-water swimmer swims poorly on an under-water plane and stops swimming when the plane is absent.

3.2.2 Under-Water Swimmer Characterization

To improve the performance, a stiff frame was attached to the two ends of the soft magnetic composite sheet, forming an under-water swimmer. It was observed that the under-water swimmer deforms like a traveling wave when a rotating uniform magnetic field was applied along its length (plan x - z). To observe its deformation, the under-water swimmer was clamped at its frame edge and submerged in water, see **Fig. 11(a)**. Note that the swimmer's plane was perpendicular to the water surface, different with the on-water swimmer setup. However, this variation did not affect the experimental result due to the absence of water surface and buoyancy forces in this case. The swimmer was at the \tilde{x} - \tilde{z} plane of the container coordinate frame while the applied uniform magnetic field was at the \tilde{x} - \tilde{y} plane, see **Fig. 11(b)**. The magnetic field had an amplitude of 9 mT and rotated at 40 Hz in the counter-clockwise direction in the \tilde{x} - \tilde{y} plane. The camera recorded the top-view scene at 400 frames per second, and the frames of one field rotating cycle are shown in **Fig. 11(c-l)**. It is evident in these frames that the swimmer deformed to approximate a traveling wave moving from its right end towards its left end.

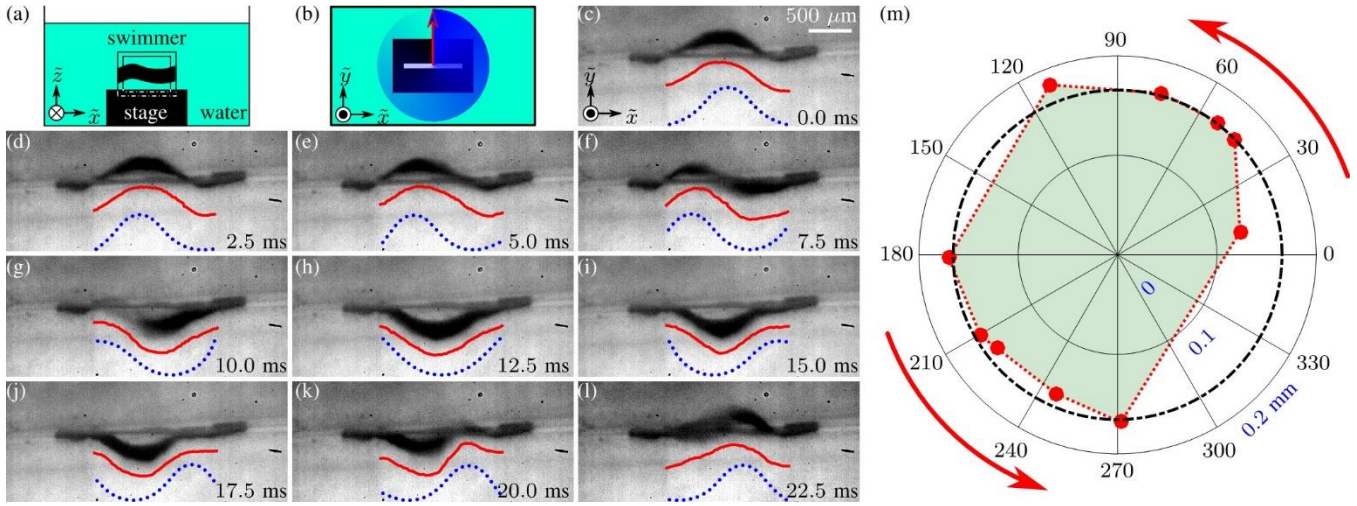


Fig. 11: Shape observations of an under-water swimmer in a rotating uniform magnetic field and the resultant characterization results. The swimmer was fixed as shown in (a) and the magnetic field was applied in the \tilde{x} - \tilde{y} plane in a counter-clockwise direction, see (b). Ten consecutive top-view (\tilde{x} - \tilde{y} plane) frames captured in one field rotation cycle are displayed in (c-l) chronologically. The lines represent the extracted swimmer shape profiles. The dots plot the simulated swimmer profiles using a pinned-pinned boundary condition as an approximation. The swimming characterization results are shown in (m). The dashed circle represents the equivalent circle with the magnitude $R_e = 166 \mu\text{m}$.

The under-water swimmers can also be characterized by Euler-Bernoulli beam theory. The stiff frame creates a fixed-fixed boundary condition for the magnetic sheet. A fixed end can exert a torque and a force on the sheet, involving three variables: the torque amplitude, the force amplitude, and the force direction. These variables are unknown and cannot be measured or derived at current stage. Thus, a pinned-pinned boundary condition was used as an approximation with the sacrifice of ignoring the slopes at the sheet ends. With this simplification, the swimmer shapes were predicted from first principles, using the proposed numerical strategy. Note that the weight of the swimmer was not considered since it pointed along the swimmer width in this case. These results qualitatively described what the swimmer shape should look like and were plotted in **Fig. 11(c-l)**.

The shape profiles of the under-water swimmer were extracted from the frames and plotted as the red lines in **Fig. 11(c-l)**. The proposed TWC analysis was performed on these profiles to characterize the

swimmer swimming performance. The resultant TWC vector of each profile is plotted by red dots in **Fig. 11(m)**, together with a dashed black circle denoting the equivalent circle with an amplitude of $166 \mu\text{m}$. The values of the characterization parameters are summarized in **Table 1**. The relatively large ϵ means that the amplitude values of the swimmer deformation were close to the equivalent circle with small variations. While the relatively large ψ suggests an evident nonuniformity in the phase angle, which agrees with the two large line segments in **Fig. 11(m)**.

Table 1 suggests that the on-water swimmer at water surface in the idealized case is the closest approximation to a TSW, exhibiting the ‘best’ swimming performance. The distortion in the magnetization and the applied magnetic field for an on-water swimmer deteriorate its swimming performance and therefore reduce ϵ while increase ψ . An on-water swimmer hardly swims under water because the absence of the constraints provided by surface tension. A proposed under-water swimmer successfully ameliorates the performance, as indicated by more favorable values of ϵ and ψ . It is also concluded that ψ is the dominating parameter that dictates the swimming performance of a swimmer.

The relative magnitude of the characterization parameters between the two experimental cases shows that the phase angle of the on-water swimmer changes more consistently, while the swimming magnitude of the under-water swimmer has a smaller variation. The on-water swimmer was free to shrink and expand at an air-water interface, resulting in a more variable deformation amplitude.

Additionally, the distorted magnetic field shifted by \vec{B}_s exacerbated the magnitude variance of the TWC vectors. In contrast, the ends of the under-water swimmer were fixed and resulted in a higher ϵ value. However, the temporal uniformity of the under-water swimmer is worse than the one of the on-water swimmer, as exhibited by the two large sectors in **Fig. 11(m)**. The reason is that the sheet is longer than the frame, forming an initial curvature on its body. When the sheet needs to deform from a ‘convex’ shape to a ‘concave’ one, it needs to overcome the constraint posed by the shorter frame, which delays the phase angle change. Once the sheet has overcome this constraint, it then moves quickly to ‘catch up’ the magnetic field, causing a nonuniform phase angle and a larger ψ value. Overall, the proposed characterization parameters provide a meaningful criterion to evaluate and compare the swimming performance of different swimmers in various scenarios.

3.2.3 Demonstration of Generating Propulsive Forces

There is no surface tension force on under-water swimmers. As a result, the swimmers tend to roll when a rotating magnetic field is applied. This rolling trend, if not counteracted, prevent under-water swimmers from generating traveling wave like deformation in rotating uniform magnetic fields. Here, experiments are presented to demonstrate that under-water swimmers can generate propulsive forces for self-driving and moving loads, when their headings are externally constrained. Fully controlled undulatory swimming of under-water swimmers will be investigated in future research.

As a proof-of-concept, an under-water swimmer moved in the presence of a rotating uniform magnetic field when it was submerged in water and one side-edge of its frame was pinned to the water surface. Two more stiff frames were taped to both the front and the back of the swimmer to dampen its oscillation in a rotating magnetic field, see **Fig. 12(a)**. In this configuration, this swimmer stayed right beneath the air-water interface and kept a vertical pose. This setup was designed specifically to constrain the swimmer orientation for easy actuation. A rotating uniform magnetic field was applied in the \tilde{x} - \tilde{y} plane with an amplitude of 11.5 mT and a frequency of 40 Hz. A top-view camera (60 Hz, FOculus)

recorded the scene and the swimmer centroid sequence are shown in **Fig. 12(b)**. It is shown that the swimmer moved in a rotating magnetic field and could reverse its locomotion direction once the magnetic field rotated in the opposite direction. Since the swimmer was pinned to the air-water interface, this demonstration did not show a fully controlled swimming motion, but it sufficed to reveal the propulsive forces created by the undulatory deformation of the under-water swimmer. In practical applications, the under-water swimmer should be able to take any pose in 3D space, in which case its alignment with the actuating magnetic field remains as a challenge and will be investigated in future research.

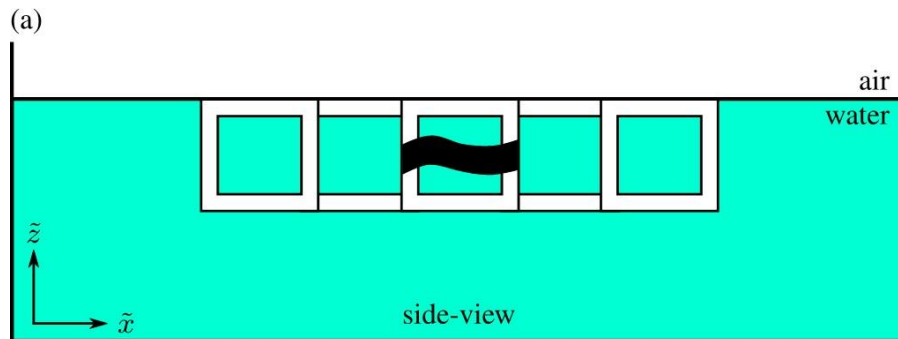
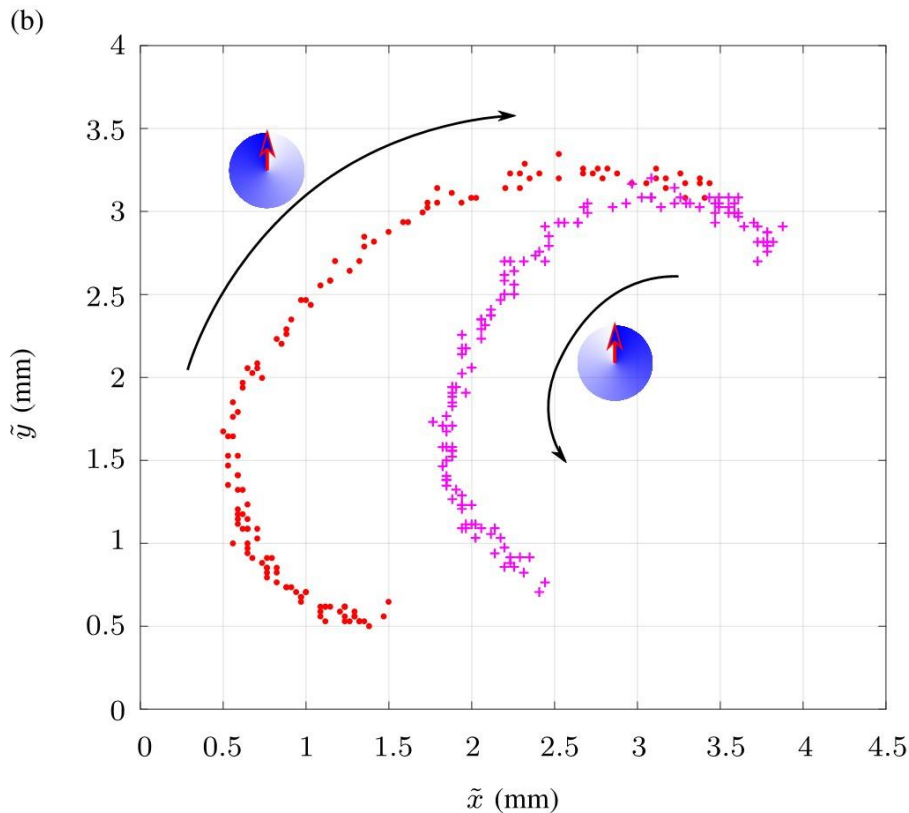


Fig. 12: Proof-of-concept demonstration of an under-water swimmer generating propulsive forces in a rotating uniform magnetic field. The swimmer was pinned to the water surface by one of its side edge, see (a). The swimmer centroids in a back-and-forth movement are plotted in (b) by dots and crosses. This experiment is also shown in **Movie 4**.



In another experiment, two under-water swimmers were attached to an acrylic beam, which was mounted on a needle through a central hole. The whole setup was submerged in distilled water. A rotating uniform magnetic field was applied within a plane that was perpendicular to the beam and therefore parallel with the long sides of both swimmers. Under the actuation of a rotating magnetic field

(20 mT), the two swimmers deformed to generate propulsive forces, that pushed the beam to rotate. When the rotating direction of the magnetic field was reversed, the rotating direction of the beam also switched. The setup of this experiment and the resultant angular velocity of the beam are shown in **Fig. S5**. A video of this experiment is shown in **Movie 5**.

Since the swimmers were pre-deformed, they had nonzero net magnetic moments and could experience magnetic forces and torques in the applied magnetic field. These effects on the net magnetic moments could add to the beam rotation, but their contributions are believed to be negligible. Firstly, the coil system was used to create a rotating uniform magnetic field. As a result, the field gradient within the workspace was near zero, if not zero due to tolerances, and consequently the magnetic forces were minimal. For any time instance within one period of field rotation, there always existed another instance when the field pointed the opposite direction with the same amplitude. Thus, the net torque on the whole device over one period should remain zero. Secondly, **Movie 5** clearly shows that the beam rotated faster as the field rotation frequency increased, and the beam changed its rotation direction when the field rotation direction is reversed. For a given period of time, neither the net magnetic torque or the net magnetic force on the device was sensitive to this frequency or direction change of the actuating field. In contrary, the undulatory deformation of swimmers was directly affected by the frequency and the direction of field rotation. Thus, it is safe to conclude that the propulsive force that rotated the beam mainly came from the undulatory deformation of the two under-water swimmers.

To visualize the propulsive forces generated by the swimmer deformation, microbeads were mixed in the water in the shape observation setup. These suspended microbeads indicated the flow disturbance caused by the swimmer deformation. A particle image velocimetry (PIV) was performed to extract the flow movement using the PIVlab tool proposed by Thielicke et al.^{42,43} A rectangle enclosing the swimmer was excluded from the analysis to avoid any interferences due to the swimmer body deformation. Each frame in one field rotation cycle was compared with its immediate next frame. The ten results were averaged and shown in **Fig. 13**. The swimmer pushed and pulled the surrounding microbeads periodically. Although the microbeads did not move parallel with the swimmer, they obtained a net movement along axis x after one period of field rotation. And the net movement direction could be easily reversed by rotating the magnetic field in the opposite direction.

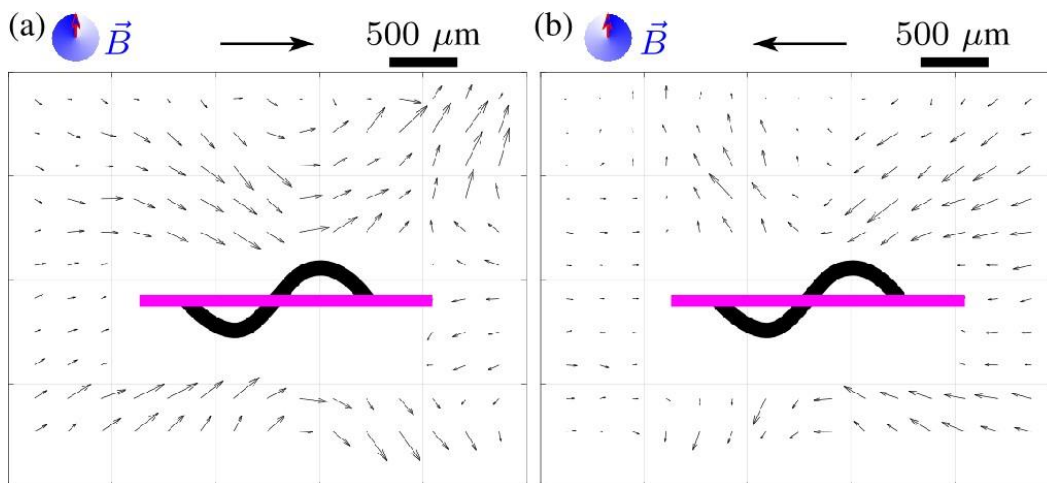


Fig. 13: Fluid disturbance caused by the swimmer deformation. The averaged PIV results across one field rotation cycle are shown in (a) and (b), corresponding to a clockwise rotating field and a counter-clockwise one, respectively. The arrow above a frame denote the travelling direction of the swimmer deformation.

The above experiments demonstrated that the traveling wave component (TWC) in the sheet deformation of under-water swimmers created propulsive forces that could not only propel the swimmer itself to swim, but also carry a certain amount of load. Therefore, the under-water swimmer can be potentially used as a power unit for miniature devices to harvest energy from ambient magnetic field and convert it to mechanical propulsion, enabling locomotion in future microdevices similar with the submarine envisioned in *Fantastic Voyage* (1966).

4 Conclusions

This work models and characterizes an undulatory swimming sheet, whose swimming ability is enabled by its magnetic elastic composite material bearing a sinusoidal magnetization profile. In a rotating uniform magnetic field, the sheet deforms into traveling wave like shapes, which interact with the surrounding liquid and generate propulsive forces for a non-holonomic bidirectional swimming gait. The sheet is made into on-water swimmers and under-water swimmers. The deformation of an on-water swimmer is modeled from underlying physical principles, and the model accuracy is endorsed by a comparison between the observed and the predicted deformations. An autonomous path-following task demonstrates the maneuverability of the on-water swimmer. A proof-of-concept experiment shows the capability of generating propulsive forces of the under-water swimmer that is submerged in water. The traveling wave component (TWC) is extracted from a swimmer deformation and analyzed to describe its spatiotemporal similarity with a traveling sinusoidal wave (TSW), providing an index to compare the swimming performance of a swimmer.

The modeling and characterization of the swimming behavior of the soft magnetic composite sheet provide an insight into the underlying physics of the undulatory swimming gait. The undulatory swimming is not time-reversible and therefore not limited by Purcell's scallop theorem, allowing it to function in the low Reynolds number regime in theory. From preliminary tests, both on-water and under-water swimmers were able to maintain their functionalities in fluids with viscosity values up to $3 \text{ mm}^2/\text{s}$ (or cSt in the CGS system of units), which is roughly the viscosity of whole blood. In a fluid with a high viscosity, the ideal input rotational field frequency for a given field strength will become lower.

The swimmer shown here could be deployed as microrobotic agents to work in small and constrained environments, or integrated into a larger device as a unit to harvest energy from an applied magnetic field and convert it into mechanical energy to induce locomotion. As discussed by Hu et al, this swimming sheet can be potentially made biocompatible by adding a thin outer layer of biocompatible polymer without sacrificing any of its functionalities, allowing it to be deployed in biomedical tasks such as drug delivery.⁷ The knowledge obtained in this study can potentially guide the design and optimization of future swimming devices. The control and characterization of the under-water swimmer will be investigated in the future research, together with the possibility of the integration of the swimmer into larger robotic devices.

5 Acknowledgement

This work was supported by the Natural Sciences and Engineering Research Council of Canada through the Discovery Grant Program 2014-04703.

6 Author Disclosure Statement

No competing financial interests exist.

7 References

1. Anton SR, Sodano HA. A review of power harvesting using piezoelectric materials (2003-2006). *Smart Mater Struct.* 2007;16(3):R1-R21.
2. Mohd Jani J, Leary M, Subic A, et al. A Review of Shape Memory Alloy Research, Applications and Opportunities. *Mater Des.* 2014;56:1078-1113.
3. Carpi F, Kornbluh R, Sommer-Larsen P, et al. Electroactive polymer actuators as artificial muscles: are they ready for bioinspired applications? *Bioinsp Biomim.* 2011;6(4):045006.
4. Diller E, Zhuang J, Lum G, et al. Continuously Distributed Magnetization Profile for Millimeter-Scale Elastomeric Undulatory Swimming. *Appl Phys Lett.* 2014;104(17).
5. Schmauch MM, Mishra SR, Evans BA, et al. Chained iron microparticles for directionally controlled actuation of soft robots. *ACS Appl Mater Interfaces.* 2017;9(13):11895–11901.
6. Lum GZ, Ye Z, Dong X, et al. Shape-Programmable Magnetic Soft Matter. *Proc Natl Acad Sci USA.* 2016;113(41):E6007-E6015.
7. Hu W, Lum GZ, Mastrangeli M, et al. Small-scale soft-bodied robot with multimodal locomotion. *Nature.* 2018:25443.
8. Zhang L, Abbott J, Dong L, et al. Artificial bacterial flagella: Fabrication and magnetic control. *Appl Phys Lett.* 2009;94:064107.
9. Diller E, Sitti M. Three-Dimensional Programmable Assembly by Untethered Magnetic Robotic Micro-Grippers. *Adv Funct Mater.* 2014;24:4397-4404.
10. Zhang J, Diller E. Tetherless Mobile Micrograsping Using a Magnetic Elastic Composite Material. *Smart Mater Struct.* 2016;25(11):11LT03.
11. Zhang J, Onaizah O, Middleton K, et al. Reliable Grasping of Three-Dimensional Untethered Mobile Magnetic Microgripper for Autonomous Pick-and-Place. *IEEE Robot Autom Lett.* 2017;2(2):835-840.
12. Zhang J, Diller E. Millimeter-Scale Magnetic Swimmers Using Elastomeric Undulations. In: *IEEE/RSJ Int. Conf. Intell. Robots Syst.* Hamburg, Germany; 2015:1706-1711.
13. Zhang J, Jain P, Diller E. Independent Control of Two Millimeter-Scale Soft-Bodied Magnetic Robotic Swimmers. In: *IEEE Int. Conf. Robot. Autom.* ; 2016:1933-1938.
14. Huang H-W, Sakar MS, Petruska AJ, et al. Soft Micromachines with Programmable Motility and Morphology. *Nat Commun.* 2016;7:1-10.
15. Xu T, Yu J, Yan X, et al. Magnetic Actuation Based Motion Control for Microrobots: An Overview. *Micromachines.* 2015;6(9):1346-1364.
16. Tottori S, Zhang L, Qiu F, et al. Magnetic Helical Micromachines: Fabrication, Controlled Swimming, and Cargo Transport. *Adv Mater.* 2012;24:811-816.
17. Huang TY, Sakar MS, Mao A, et al. 3D Printed Microtransporters: Compound Micromachines for Spatiotemporally Controlled Delivery of Therapeutic Agents. *Adv Mater.* 2015;27(42):6644-6650.
18. Breger J, Yoon C, Xiao R, et al. Self-Folding Thermo-Magnetically Responsive Soft Microgrippers. *ACS Appl Mater Interfaces.* 2015;7(5):3398-3405.

19. Fusco S, Huang H-W, Peyer KE, et al. Shape-Switching Microrobots for Medical Applications: The Influence of Shape in Drug Delivery and Locomotion. *ACS Appl Mater Interfaces*. 2015;7:6803-6811.
20. Mhanna R, Qiu F, Zhang L, et al. Artificial bacterial flagella for remote-controlled targeted single-cell drug delivery. *Small*. 2014;10(10):1953-1957.
21. Gao W, Wang L, Wang X, et al. Magnetic Driving Flower-like Soft Platform: Biomimetic Fabrication and External Regulation. *ACS Appl Mater Interfaces*. 2016;8(22):14182-14189.
22. Leong T, Randall C, Benson B, et al. Tetherless Thermobiochemically Actuated Microgrippers. *Proc Natl Acad Sci USA*. 2009;106(3):703-708.
23. Li J, Ávila BE-F de, Gao W, et al. Micro/Nanorobots for Biomedicine: Delivery, Surgery, Sensing, and Detoxification. *Sci Robot*. 2017;2:1-10.
24. Sitti M, Ceylan H, Hu W, et al. Biomedical Applications of Untethered Mobile Milli/Microrobots. *Proc IEEE*. 2015;103(2):205-224.
25. Peyer K, Zhang L, Nelson BJ. Bio-Inspired Magnetic Swimming Microrobots for Biomedical Applications. *Nanoscale*. 2013;5(4):1259-1272.
26. Yan X, Zhou Q, Vincent M, et al. Multifunctional biohybrid magnetite microrobots for imaging-guided therapy. *Sci Robot*. 2017;2(12):eaq1155.
27. Chung S, Dong X, Sitti M. Three-Dimensional Heterogeneous Assembly of Coded Microgels Using An Untethered Mobile Microgripper. *Lab Chip*. 2015;15(7):1667-1676.
28. Erb RM, Martin JJ, Soheilian R, et al. Actuating Soft Matter with Magnetic Torque. *Adv Funct Mater*. 2016;26(22):3859-3880.
29. Gelebart AH, Jan Mulder D, Varga M, et al. Making Waves in A Photoactive Polymer Film. *Nature*. 2017;546(7660):632-636.
30. Moeller MP, Schaeppli A, Buholzer P, et al. *Sepios: Riding the Wave of Progress.*; 2014.
31. Cheang UK, Kim MJ. Fabrication and control of simple low Reynolds number microswimmers. *Appl Phys Lett*. 2016;109(3):1-6.
32. Palagi S, Mark AG, Reigh SY, et al. Structured light enables biomimetic swimming and versatile locomotion of photoresponsive soft microrobots. *Nat Mater*. 2016;15:647-653.
33. Huang C, Lv J, Tian X, et al. Miniaturized Swimming Soft Robot with Complex Movement Actuated and Controlled by Remote Light Signals. *Sci Rep*. 2015;5:17414.
34. Palagi S, Jager EWH, Mazzolai B, et al. Propulsion of swimming microrobots inspired by metachronal waves in ciliates: from biology to material specifications. *Bioinspir Biomim*. 2013;8:046004.
35. Setter E, Bucher I, Haber S. Low-Reynolds-number swimmer utilizing surface traveling waves: Analytical and experimental study. *Phys Rev E Stat Nonlin Soft Matter Phys*. 2012;85(6):066304.
36. Lauga E, Powers TR. The hydrodynamics of swimming microorganisms. *Rep Prog Phys*. 2009;72:096601.
37. Taylor G. Analysis of the swimming of microscopic organisms. *Proc R Soc A*. 1951;209:447-461.
38. Zhuang J, Wright Carlsen R, Sitti M. pH-Taxis of Biohybrid Microsystems. *Sci Rep*. 2015;5:11403.
39. Song YS, Suhr SH, Sitti M. Modeling of the Supporting Legs for Designing Biomimetic Water Strider Robots. In: *IEEE Int. Conf. Robot. Autom.* ; 2006:2303-2310.
40. Martel S, Felfoul O, Mathieu J-B, et al. MRI-Based Medical Nanorobotics Platform for the Control of Magnetic Nanoparticles and Flagellated Bacteria for Target Interventions in Human Capillaries. *Int J Robot Res*. 2009;28(9):1169-1182.
41. Ullrich F, Bergeles C, Pokki J, et al. Mobility Experiments with Microrobots for Minimally

- Invasive Intraocular Surgery. *Invest Ophthalmol Vis Sci*. 2013;54(4):2853-2863.
42. Thielicke W, Stamhuis EJ. PIVlab - Towards User-friendly, Affordable and Accurate Digital Particle Image Velocimetry in MATLAB. *J Open Res Softw*. 2014;2(1):e30.
 43. Thielicke W. The Flapping Flight of Birds: Analysis and Application. *PhD Thesis*. 2014.

Untethered miniature soft robots: Modeling and design of a millimeter-scale swimming magnetic sheet (Supplementary Information)

Swimmer Fabrication

Both on-water and under-water swimmers were fabricated using a replica molding technique with negative molds, whose fabrication process is detailed in **Fig. S1**. First, the geometries of the magnetic elastic composite strip and the stiff frame were defined in AutoCAD and then written on a photomask using a mask writer (Heidelberg μ PG 501 Maskless Aligner), see **Fig. S1(a)**.

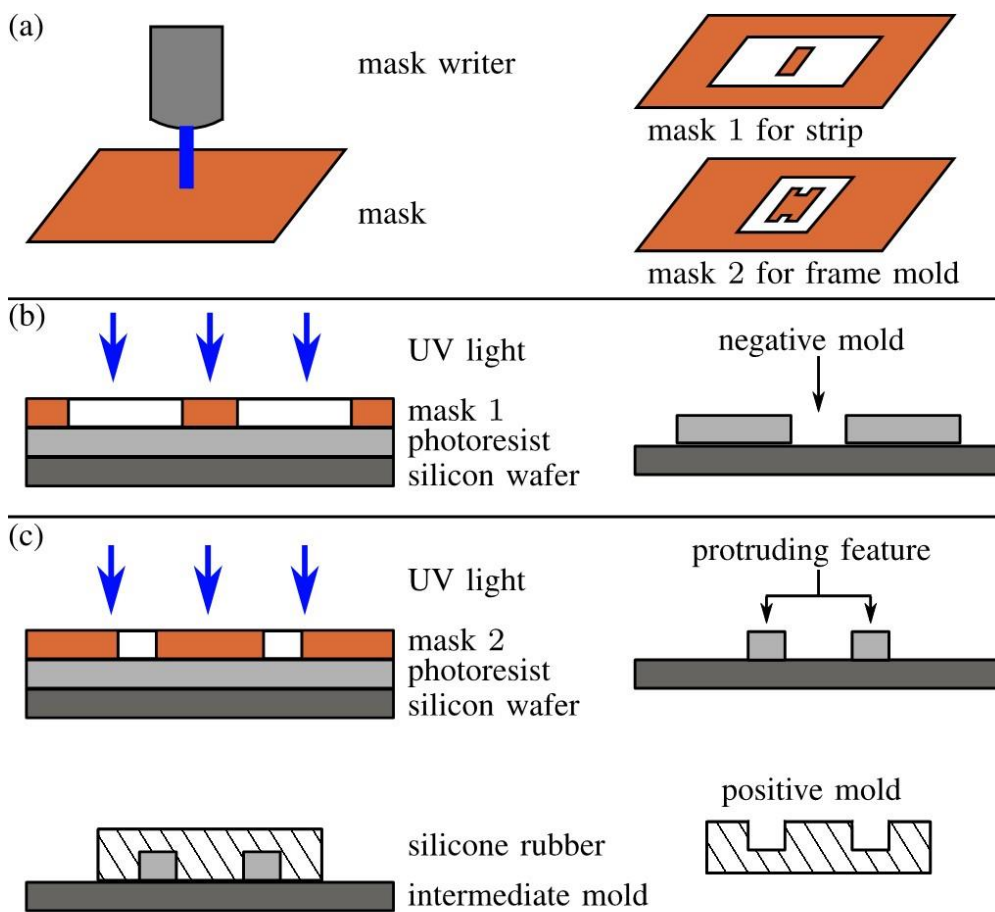


Fig. S1: Illustrations of the fabrication process of the molds used to make on-water and under-water swimmers. Masks were made by directly writing in (a), and then placed on top of photoresist to control the exposure region, see (b) and (c). The exposed photoresist remained on the wafer, forming the desired molds. An additional step was used to fabricate a soft rubber mold for the stiff frame in (c).

These geometric features were then transferred to a layer of photoresist (SU-8 2025, MicroChem) through a standard photolithography process. A layer of photoresist was spin coated on a 3 inches silicon wafer (UniversityWafer), soft baked at 65 °C, and then exposed to ultra-violet (UV) light with the corresponding mask on top of it, see **Fig. S1(b)** and **(c)**. A post-exposure bake (PEB) at 95 °C was performed to cross-link the exposed portion of the photoresist. After being developed in an organic solvent solution (SU-8 Developer, MicroChem), the cross-linked portion of the photoresist stayed on the

wafer while the rest was wasted away, forming the desired negative (concave) molds. The molds were then baked at 170 °C for 10 minutes. The baking time and exposure dosage were set according to the photoresist datasheet based on the desired mold thickness T .

As shown in **Fig. S1(c)**, the fabrication of the mold for the stiff frame used the cross-linked photoresist as an intermediate positive (protruding) mold to create a negative mold using the silicone rubber (Mold Max 20, Smooth-On). This is because both the cross-linked photoresist and the frame are stiff, making it problematic to directly use the photoresist mold to create the frame. Thus, a soft rubber mold copied the feature from the photoresist mold and was made to bear the frame. The geometric dimension of the frame is shown in **Fig. S2**.

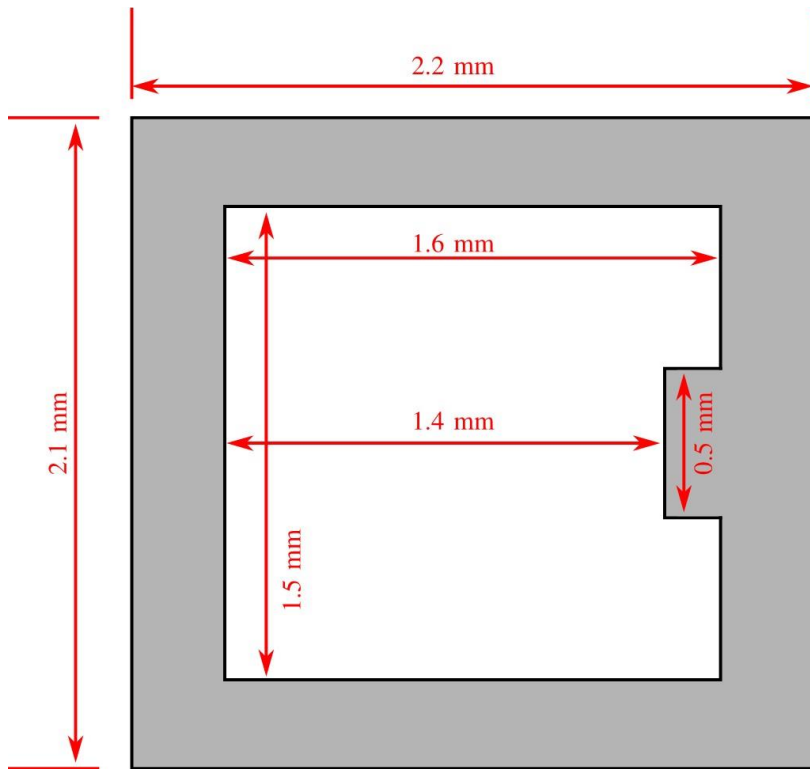


Fig S2: The geometric dimension of the frame used by under-water swimmers. The frame is 30 μm thick.

This process allows easy modification of the geometries of the strip and the frame, facilitating the fabrication of swimmers of different sizes. Ecoflex 0050 (Smooth-On) is chosen as the basic polymer material for the soft magnetic composite for its excellent softness and elasticity (100% modulus of 12 psi). This soft polymer is mixed with permanent magnetic powders (MQFP-15-7, NdPrFeB, Magnequench) at a 1:1 mass ratio. The magnetic powders have a nominal diameter value that is less than 10 μm .

Electromagnetic Coils

A custom-built 3D electromagnetic coil system provided the magnetic field used in the autonomous path-following experiment of on-water swimmers. The coil system has 3 pairs of coils nested along the 3 orthogonal axes of a 3D Cartesian coordinate system. Each pair of coils was arranged to approximate a

Helmholtz coil configuration. All coils are supported by analog servo drives (30A8, Advanced Motion Controls), which connect to a computer through a multifunction analog/digital I/O board (Model 826, Sensoray).

A custom-built 2D electromagnetic coil system was used in the observation of the on-water swimmer deformation. This 2D coil system is identical with the 3D coil system except that the inner-most pair of coils was removed to accommodate a larger workspace.

Parameter Measurement

In order to measure the Young's modulus E of the soft magnetic composite, two sheets ($1.38 \times 4.61 \times 0.134 \text{ mm}^3$ and $1.36 \times 4.66 \times 0.118 \text{ mm}^3$) were fabricated but not magnetized, and then attached to stiff acrylic stages, forming cantilever beams as shown in **Fig. S3(a)**. A micro-force sensing probe (FT-S100 probe, FemtoTools) mounted on a robotic arm (FT-RS1000-SCOPE, FemtoTools) applied a perpendicular point force \vec{F} on the sheet. The bending moment profile Q of the sheet is drawn in **Fig. S3(b)** and is described as

$$Q(x) = -Fx + FL_p \quad (\text{S1})$$

where F is the force amplitude and L_p is the length from the fixed point of the sheet to \vec{F} . When the sheet deformation is small, its curvature κ can be approximated as

$$\kappa = d^2\omega/dx^2 \quad (\text{S2})$$

Substituting the expressions of Q and κ into **Eq. (14)**, the displacement can be calculated with the known boundary conditions of $\omega(0) = 0$ and $d\omega(0)/dx = 0$. The result is

$$\omega(x) = F \cdot (-x^3 + 3Lx^2) \cdot (6EI)^{-1} \quad (\text{S3})$$

At the point of \vec{F} , the displacement is

$$\omega(L_p) = (FL_p^3) \cdot (3EI)^{-1} \quad (\text{S4})$$

Finally, there is

$$E = \frac{4L_p^3}{WT^3} \cdot \frac{F}{\omega} \quad (\text{S5})$$

Using **Eq. (S5)**, E can be calculated after measuring the F versus ω , i.e., the slope in **Fig. S3(c)**.

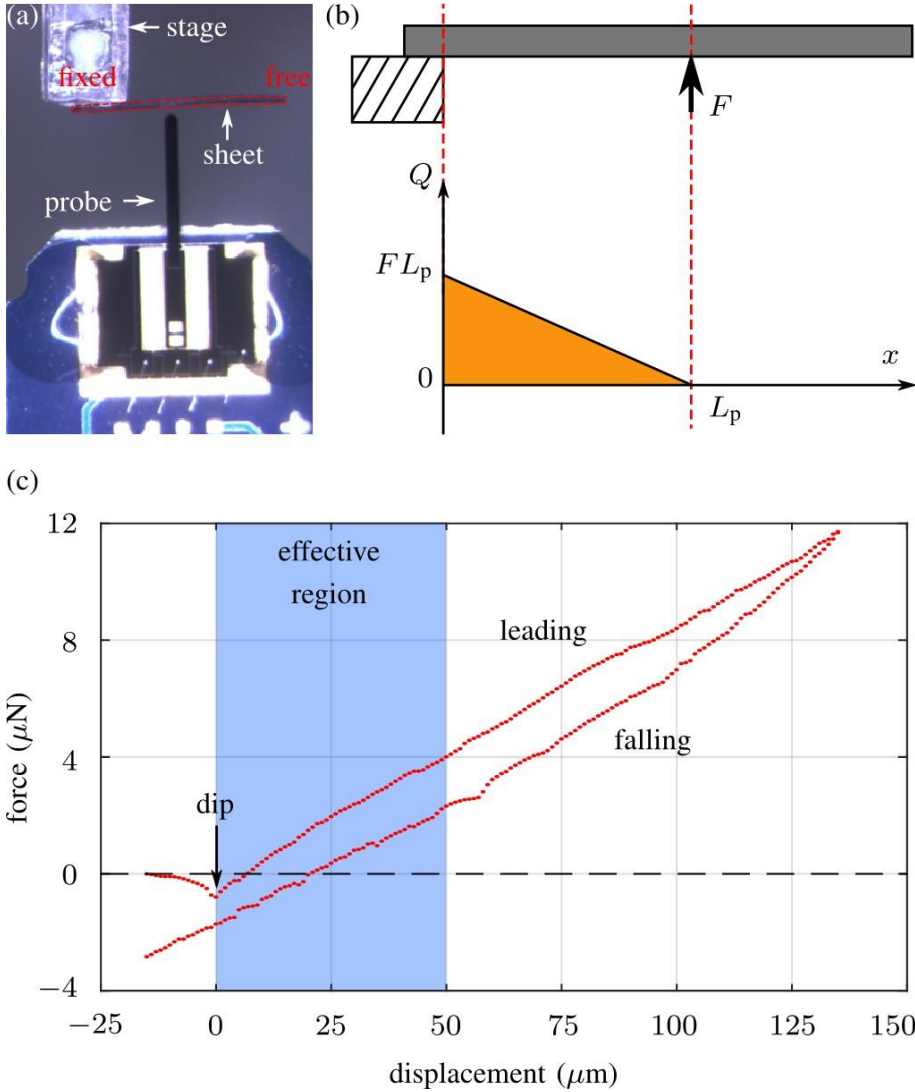


Fig. S3: Measurement of the Young's modulus E of the soft magnetic composite. A top-view photograph of the measurement setup is shown in (a), where the sheet is marked out by red dashed lines. The bending moment Q caused by the point force F is illustrated in (b). The data of one example trial is shown in (c). The dip caused by the mutual attraction between the probe and the sheet is marked out. Only the data within the blue region is used in the result calculation.

Here, the force probe was initially placed near the sheet, and then pushed perpendicularly towards the sheet. After contact was detected, the force probe continued to push the sheet to a certain distance, and then retrieved back to its original position. During this process, the force F and displacement ω of the probe were recorded. The experimental data of one representative trial is plotted in **Fig S3(c)**. When the probe moved close enough to the sheet, the sheet was pulled to the probe by static electricity, causing the force reading of the probe to drop, see the dip in **Fig S3(c)**. Note that the derivation of **Eq. (S5)** requires the sheet deformation to be small. Therefore, only the data within a range of $50 \mu\text{m}$ after the contact was used to calculate a best fit linear regression relationship between F and ω . The results of five trials for the two sheets are summarized in **Table S1**. From these experimental results, the Young's modulus E of the magnetic elastic composite material was measured to be 0.165 MPa .

Table S1: Measured Young's Modulus Values (Data Unit is MPa)

Trial Index	Swimmer 1		Swimmer 2	
	leading	falling	leading	falling
1	0.143	0.122	0.186	0.160
2	0.155	0.138	0.185	0.159
3	0.168	0.150	0.198	0.159
4	0.170	0.151	0.202	0.174
5	0.158	0.154	0.205	0.172

Simulation Algorithm

The proposed numerical algorithm to iteratively predict the swimmer shapes in the presence of a known magnetic field is explained using the pseudocode in **Algorithm 1**. One example of the simulated swimmer shape is shown in **Fig. S4(a)**. The overall bending moment profile of the swimmer body and the bending moments caused by different components are plotted in **(b-d)**. It is shown that the bending moment and the surface tension counteract each other and play the most important role in deciding the overall bending moment profile.

Algorithm 1: Swimmer Shape Simulation

1. **procedure** SIM_SHAPE($\vec{M}(s), \vec{B}$) % $\vec{M}(s)$: magnetization profile. \vec{B} : magnetic field
2. specify n and N % n : number of simulation points. N : iteration step size
3. specify e % e : convergence tolerance
4. set $\omega(s)$, $\alpha(s)$, and $\kappa_{\text{pre}}(s)$ to be all zeros % α : simulation point angle
5. specify L , W , and T % swimmer length L , width W , and thickness T
6. calculate $\Delta m = M \cdot (W \cdot T \cdot L/n)$ % magnetic moment of each simulation point
7. **do**
8. calculate $\theta_t(s)$ from $\omega(s)$ using Eq. (16)
9. calculate $F_b(s)$, $F_{t, \text{len}, v}(s)$, $F_{t, \text{wid}, v}(s)$, and $F_{t, \text{wid}, h}(s)$ from $\theta_t(s)$ using Eq. (3-6)
10. $\beta(s) = \angle \vec{B} - (\alpha_{\text{pre}}(s) + \angle \vec{M}(s))$ % angle between \vec{B} and local magnetic moment
11. $\tau(s) = \Delta m \cdot |\vec{B}| \sin \beta(s)$ % magnetic torque profile
12. calculate $Q(s)$ from forces and torques using Eq. (7-13) % bending moment
13. calculate $\kappa(s)$ from $Q(s)$ using Eq. (14) % curvature of the swimmer body
14. $\Delta \kappa(s) = (\kappa_{\text{new}}(s) - \kappa_{\text{pre}}(s))/N$
15. calculate $\omega(s)$ and $\alpha(s)$ based on $\kappa_{\text{new}}(s) = \kappa_{\text{pre}}(s) + \Delta \kappa(s)$
16. **do**
17. re-calculate F_b , $F_{t, \text{len}, v}$, $F_{t, \text{wid}, v}$, and $F_{t, \text{wid}, h}$
18. rotate and/or vertically shift swimmer to zero net force and torque, and update $\omega(s)$ and $\alpha(s)$ correspondingly
19. **while** swimmer experiences nonzero net external force or torque
20. **while** the $\omega(s)$ change in this iteration is larger than e % loop until it converges
21. **return** $\omega(s)$

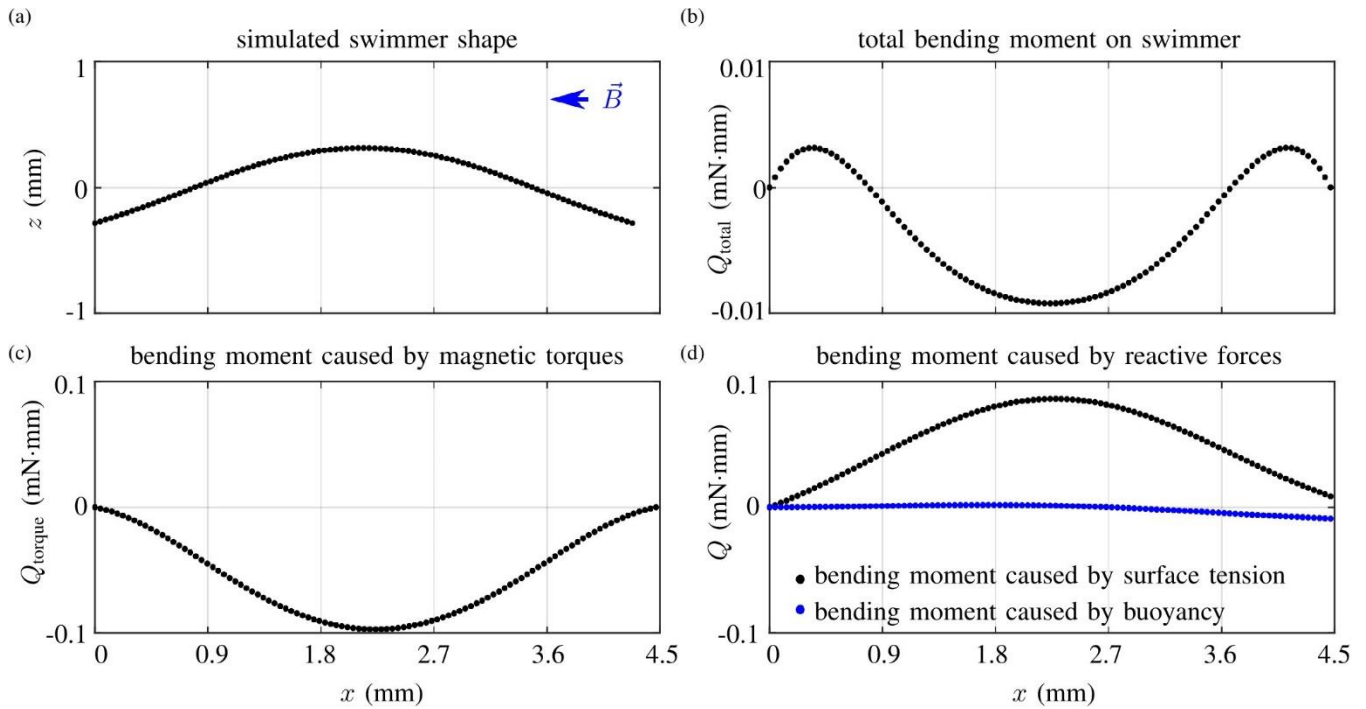


Fig. S4: One example of swimmer shape simulation. The simulated swimmer shape is plotted in (a), with its corresponding bending moment profile shown in (b). The bending moment caused by the active component, i.e., the magnetic torques, and the reactive components, i.e., surface tension and buoyancy, are plotted in (c) and (d), respectively.

Under-Water Swimmer Propulsion Demonstration

An experiment was set up to experimentally demonstrate that the undulatory deformation of under-water swimmers could generate propulsive forces that could not only move themselves but also carry a certain load. In this experiment, two under-water swimmers were mounted at the two ends of a 50 mm long acrylic beam. Each end of the beam had two fingers that provided constraints to the mounted under-water swimmers. The beam was mounted on a pole that penetrated through its central circular opening. A photo of the setup is shown in **Fig S5(a)**.

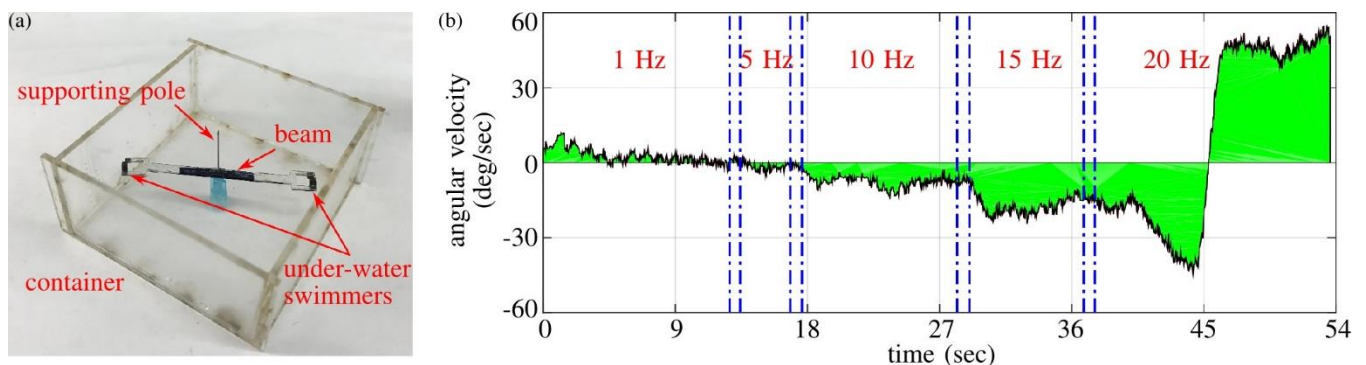


Fig. S5: An experimental demonstration of the capability of generating propulsive forces of under-water swimmers. A photo of the experimental setup is shown in (a). Note that the container was fully filled with liquid in the experiment. The angular velocity data of the beam in the experiment is shown in (b). The orientation angle of the beam was extracted from every frame of the experimental video and then used to calculate the angular velocity. A moving-average filter of a window size of 45 (corresponding to 1.5 sec in experiment) was applied before the calculation.

When a rotating uniform magnetic field was applied in a plane that is parallel with the under-water swimmers, i.e., perpendicular to the beam, the two swimmers deformed into undulatory shapes and the traveling directions of their deformation profiles were opposite to each other. As a result, the propulsive forces caused by their undulatory deformations had anti-parallel directions. Similar with a mill, the two swimmers pushed the beam to rotate. As the rotation frequency of the actuating magnetic field changed, the amplitudes of the propulsive forces varied correspondingly, altering the angular velocity of the beam. The angular velocity data of the beam in this experiment is plotted in **Fig S5(b)**.